Penning-trap-assisted decay spectroscopy studies of neutron-rich nuclei in the A = 110 region

by
Juho Rissanen

Academic Dissertation
for the Degree of
Doctor of Philosophy

To be presented, by permission of the
Faculty of Mathematics and Natural Sciences
of the University of Jyväskylä,
for public examination in Auditorium FYS-1 of the
University of Jyväskylä on September 23, 2011
at 12 o'clock noon

Jyväskylä, Finland
September 2011

Preface

The work reported here has been carried out in the IGISOL group during the years 2006-2011 at the Department of Physics in the University of Jyväskylä, Finland.

I would like to thank my supervisors, professor Ari Jokinen and professor Juha Äystö for the opportunity to do my thesis work in the IGISOL group and also for their guidance and support during the project. I am grateful to all the past and present IGISOL members who have participated in experiments related to this work. Special thanks go to 'the master of the trap' Dr. Tommi Eronen, 'the trap-assisted-pioneer' Dr. Sami Rinta-Antila, 'the trap builder' Dr. Veli Kolhinen, 'the computer support' MSc Jani Hakala and other group members, especially Dr. Viki Elomaa, Dr. Pasi Karvonen, and MSc Antti Saastamoinen for help in constructing the detector setups, running the experiments, and repairing the tape drive system. I wish to thank also these guys for cheerful moments during lunch breaks and conference travels. I want also thank Dr. Iain Moore for translating my language to proper English.

I want to thank Dr. Jan Kurpeta and his colleagues from the University of Warsaw for the opportunity to take part in the data analysis of the experiments I125 and I137 as well for helping me in data analysis and in interpretation of the results. I am also grateful to the whole BELEN-20 collaboration for bringing this excellent tool to Jyväskylä and for the opportunity to take part in the testing of the detector. In addition, warmest thanks go to Dr. Leszek Próchniak, Dr. Rayner Rodríguez-Guzmán, and Dr. Gary Simpson for providing their theoretical calculations for this thesis.

Finally, I want to thank my loving wife Merja for patience, support and encouragement throughout the years and my wonderful sons Patrik and Rasmus for reminding me about the life outside the laboratory.

Jyväskylä, September 2011

Juho Rissanen

Author   Juho Rissanen
                    Department of Physics
                    University of Jyväskylä
                    Finland

Supervisors   Prof. Dr. Ari Jokinen
                    Department of Physics
                    University of Jyväskylä
                    Finland

                    Prof. Dr. Juha Äystö
                    Department of Physics
                    University of Jyväskylä
                    Finland

Reviewers   Prof. Dr. Alison Bruce
                    School of Computing, Engineering and Mathematics
                    University of Brighton
                    United Kingdom

                    Dr. Michael Bloch
                    GSI Helmholtzzentrum für Schwerionenforschung GmbH
                    Darmstadt
                    Germany

Opponent   Prof. Dr. Thomas Nilsson
                    Department of Fundamental Physics
                    Chalmers University of Technology
                    Sweden

Abstract

Neutron-rich fission products have been studied by means of trap-assisted spectroscopy by using the JYFLTRAP Penning trap setup at the IGISOL facility in the Accelerator laboratory of the University of Jyväskylä. The isotopes ^{115}Ru, ^{115}Rh, and ^{114}Tc were studied via β-γ coincidence measurements from monoisotopic samples. New spectroscopic information was collected resulting in extended beta-decay schemes for ^{115}Ru and ^{115}Rh and a new beta-decay scheme for ^{114}Tc. New isomeric states in ^{115}Ru and ^{114}Tc were found and the half-lives for the ground states and isomeric states were measured. New ground and isomeric spin and parity values were suggested. Associating the $(3/2^+)$ ground state of ^{115}Ru as a 3/2[402] Nilsson state may be interpreted as a sign of an oblate ground state, which is consistent with a predicted prolate-oblate shape transition. The results are also important for r-process network calculations.

A new long-counter type neutron detector BELEN-20 was tested in connection to the JYFLTRAP setup. Probabilities for the beta-delayed neutron emission, the P_n values, for several beta-delayed neutron emitters were measured. Preliminary results show that the monoisotopic samples provided by JYFLTRAP are extremely important also for neutron spectroscopy.

The feasibility of JYFLTRAP for in-trap conversion electron spectroscopy was tested. Conversion electron spectra from trapped ^{117m}Pd, ^{118m,120m}Ag, and ^{118m}In isotopes were measured. The resultant spectra exhibited very high quality, $i.e.$ a low background level and an excellent energy resolution. In addition, the detection efficiency

and related phenomena were studied via simulations.

Acknowledgments

Contents

List of Tables

List of Figures

1 Introduction

Traps of different types have been used to study various physical phenomena for several decades. Ion traps, such as Penning or Paul traps, are making breakthroughs in nuclear physics. Both traps use electromagnetic fields to confine charged particles in a small volume, where the ions can be cooled and stored for relatively long times. In addition, eigenmotions of the trapped ions can be easily manipulated by different excitations, which can be used for selecting different isotopes according to mass, leading to a superior mass selectivity. Another advantage of using traps is that the trapped ions are floating almost freely, which can be utilized in some spectroscopic methods.

A double Penning trap setup JYFLTRAP was built several years ago for atomic mass measurements and for isobaric purification of the IGISOL beam. Masses of over 200 different isotopes have been measured with great precision [1], including Q values of superallowed beta emitters [2–6] or atomic mass values for nuclear structure studies [7–10] as examples. Nowadays, it is also commonly used as a mass selective filter for preparing monoisotopic ion samples for spectroscopic studies, pioneered in the PhD work of Sami Rinta-Antila [11, 12]. In this thesis the pioneering work of trap-assisted spectroscopy has been continued, different nuclei have been studied, and new instruments for detecting radiation from the samples purified isobarically with the JYFLTRAP setup have been introduced.

Two types of Penning-trap-assisted spectroscopy, in-trap spectroscopy and post-trap spectroscopy are dealt with in this thesis. In the former method, the radiation is detected from the trapped radioactive ions whereas in the latter method, the radioactive sample is purified isobarically with a Penning trap and the ions-of-interest are ejected and implanted into a spectroscopy setup located after the trap for subsequent spectroscopic studies. These studies included measurements with a β-γ detector setup as well as with a long counter neutron detector setup.

Within this work, six on-line experiments with the JYFLTRAP setup were performed. In the first one, hereby labeled as [Experiment 1], a feasibility of JYFLTRAP for the in-trap spectroscopy was tested. This experiment took place in 2005. The main spectroscopic results of this work are based on the data from three later

experiments, hereby labeled as [Experiment 2], [Experiment 3], and [Experiment 4]. [Experiment 2] took place in February 2008, wherein new data related to the beta decay of ^{115}Ru and to the subsequent beta decays of its daughter nuclides were collected. In [Experiment 3], which took place in October 2008, the beta decay of ^{114}Tc was measured, including also a determination of the Q_β value of the decay. In [Experiment 4], which took place in February 2011, the half-life of ^{115}Ru was measured. In addition, two experiments were performed dedicated for testing the BELEN-20 neutron detector, labeled as [Experiment 5] and [Experiment 6]. These experiments took place in November 2009 and in June 2010, respectively.

The main results of this thesis are presented in the following enclosed publications:

1. **Conversion electron spectroscopy of isobarically purified trapped radioactive ions**
   J. Rissanen, V.-V. Elomaa, T. Eronen, J. Hakala, A. Jokinen, S. Rahaman, S. Rinta-Antila, and J. Äystö
   European Physical Journal A **34**, 113, (2007).

2. **Excited states in ^{115}Pd populated in the β^- decay of ^{115}Rh**
   J. Kurpeta, W. Urban, A. Płochocki, J. Rissanen, V.-V. Elomaa, T. Eronen, J. Hakala, A. Jokinen, A. Kankainen, P. Karvonen, I. D. Moore, H. Penttilä, S. Rahaman, A. Saastamoinen, T. Sonoda, J. Szerypo, C. Weber, and J. Äystö.
   Physical Review C, **82**, 027306, (2010).

3. **New isomer and decay half-life of ^{115}Ru**
   J. Kurpeta, J. Rissanen, A. Płochocki, W. Urban, V.-V. Elomaa, T. Eronen, J. Hakala, A. Jokinen, A. Kankainen, P. Karvonen, T. Małkiewicz, I. D. Moore, H. Penttilä, A. Saastamoinen, G. Simpson, C. Weber, and J. Äystö.
   Physical Review C, **82**, 064318, (2010).

4. **Decay study of ^{114}Tc with a Penning trap**
   J. Rissanen, J. Kurpeta, V.-V. Elomaa, T. Eronen, J. Hakala, A. Jokinen, P. Karvonen, I. D. Moore, A. Płochocki, L. Próchniak, H. Penttilä, S. Rahaman, M. Reponen, A. Saastamoinen, J. Szerypo, W. Urban, C. Weber, and J. Äystö.
   Physical Review C, **83**, 011301, (2011).

5. **Penning-trap-assisted study of ^{115}Ru beta decay**
   J. Rissanen, J. Kurpeta, A. Płochocki, V.-V. Elomaa, T. Eronen, J. Hakala, A. Jokinen, A. Kankainen, P. Karvonen,I. D. Moore, H. Penttilä, S. Rahaman, A. Saastamoinen, W. Urban, C. Weber, and J. Äystö.

European Physical Journal A **47**, 97, (2011).

The author of this thesis has been the liaison person for the experiments related to the enclosed papers. The author has been a person in charge of the design and construction of the detector setups, which required modifications and additional structures in the trap extraction beam line related to [Publication 1]. The author has performed the data analysis and has written [Publication 1], [Publication 4], and [Publication 5], and participated in writing and in the data analysis of [Publication 2] and [Publication 3].

In this thesis, following a short introduction in Chapter 1, the theoretical background is given in Chapter 2. The experimental methods are described in Chapter 3. The results which are not published in the enclosed papers are discussed in Chapter 4. Chapter 5 summarizes the present work.

2 Theoretical background - formulae and selection rules for experimentalists

2.1 Motivation for spectroscopic studies on neutron-rich refractory elements

The nuclei studied in this work are located in the $A \approx 110$ mass region on the neutron-rich side of the nuclide chart. Spectroscopic studies in this region are often motivated by a rich variety of nuclear structures and shapes, but also due to a close connection to the astrophysical r process. In following subsections the above mentioned features will be briefly discussed.

2.1.1 Nuclear structure

A motivation for the studies of this work from the nuclear structure point of view is related to the nuclear shape transitions. The most deformed nuclei in the $A \approx 110$ region are the strontium and zirconium isotopes and another extreme is reached in the spherical tin isotopes, which is a typical shape for nuclei around closed shells. The cadmium isotopes close to tin are good examples of vibrational nuclei. The neutron-rich molybdenum-ruthenium-palladium isotopes are far from the magic proton or neutron numbers and therefore a vast variety of different shapes can be found. For example, the ruthenium isotopes undergo a shape transition from spherical to gamma-soft prolate shape around $N \approx 60$–70 [13–20] and therefore they have been described as transitional nuclei in the Interacting Boson Approximation (IBA) model [13, 14, 19]. In addition, the rigidity of the triaxial shapes has been predicted to increase when going towards more neutron-rich species [16, 17, 19]. Another shape transition, from gamma-soft prolate to gamma-soft oblate shape has been predicted to take place around $N \approx 70$ [21]. A similar shape transition should also take place in molybdenum and palladium isotopes. This region is a challenging test bench for different theoretical models since the exact locations of the transitions are difficult to predict and they are very sensitive to different model assumptions. Also a co-existence of oblate and prolate states has been found, for example in

palladium isotopes [22, 23].

2.1.2 Astrophysical r process

About half of the elements heavier than iron existing in the universe today are understood to originate from the astrophysical r process (rapid neutron capture - process) [24, 25]. The process takes place in an environment with a very high neutron flux leading to a rapid neutron capture on a timescale short compared to the time needed for nuclear beta decay. Neutron-rich nuclei capture neutrons until the separation energy of the next neutron becomes so small that the nuclei will be disintegrated by photons. At this point, called a waiting point, no further neutron capture can occur and the nucleus will undergo a beta decay. A sequence of neutron captures and beta decays creates heavy elements until the fission reactions enter the picture terminating the r process in the thorium-uranium region.

The basic principle of the r process is nowadays well understood but the astrophysical sites and the precise path of the process have not yet been unambiguously identified. The gross beta-decay properties ($Q_\beta, S_n, P_n, t_{1/2}$) are the main nuclear physics input when predicting the r-process path and timescale. The energies Q_β and S_n are responsible for the path and $t_{1/2}$ for the timescale of the process. When the neutron flux diminishes, the nuclei will decay towards the valley of stability by beta decay and beta-delayed neutron emission. Also the existence of isomers can affect the r-process path [26].

Since the r-process path is located far from the valley of stability, experimental measurements of the properties of nuclei along the path are very challenging. At the moment, astrophysical calculations have to rely on theoretical estimates, which are not very reliable when approaching the neutron drip line. Therefore, experiments have to be pushed forward towards the more exotic cases.

2.2 Nuclear structure models

2.2.1 Spherical and deformed shell model

The nuclear shell model is built on an assumption that a nucleon is moving independently in a central potential created by the other nucleons in the nucleus. The protons and neutrons are fermions and they obey the Pauli exclusion principle.
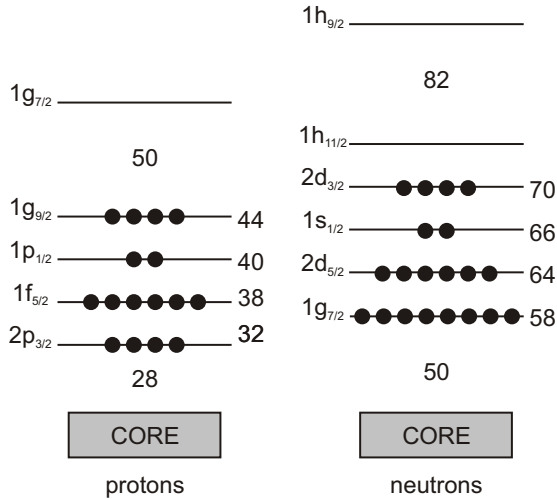
Figure 2.1: A schematic view of the spherical shell model energy levels relevant for this work. The occupation of levels (black circles) represents ^{114}Ru.

Therefore, two identical particles cannot be in the same quantum state. Originally, a simple harmonic oscillator potential was used and the correct shell-model description was achieved later when the spin-orbit interaction was included in the model. It was the needed component to explain the right magic numbers (2,8,20,28,50,82,126), where the large shell gaps are found. A review on the shell model can be found in [27].

The interaction between two nucleons is different for identical and non-identical nucleons. Identical nucleons interact strongly if they both occupy the same orbit, coupling to $J^\pi = 0^+$. This effect is called pairing. It is clearly seen in even-even nuclei, which have always 0^+ as the ground state spin. A consequence of the pairing is that the ground-state spin and parity of odd-mass nuclei are often determined by the spin and parity of the unpaired nucleon.

A weak quadrupole force between the like nucleons can produce only spherical shapes whereas the proton-neutron interaction has a large quadrupole component, proposed to be responsible for deformation. Therefore, deformed (spheroidal) shapes can be found in the regions of open shells, where neutron-proton correlations dominate over those of like nucleons. Axially symmetric deformed shapes are divided into prolate or oblate shapes, the former having the shape of an American football and the lat-

ter like a disc. In deformed nuclei the simple spherical shell model picture has to be modified. In the model introduced by Nilsson [28], the deformation is fixed beforehand and the single-particle levels are calculated from that deformation. The $(2j + 1)/2$-fold degeneracy of the spherical orbits is broken and j is no longer a good quantum number. The states are described with the asymptotic quantum numbers $\Omega^\pi[Nn_z\Lambda]$, where Ω is the projection of the single-particle angular momentum onto the symmetry axis, N is the principal quantum number, n_z is the number of oscillating quanta along the symmetry axis, *i.e.* the number of nodes in the wave function, and Λ is the projection of the orbital angular momentum l_i on the symmetry axis. The parity π is given by $(-1)^N$. An illustration of the asymptotic quantum numbers for the Nilsson model is presented in Fig. 2.5. The Nilsson diagrams for protons and neutrons relevant for this work are presented in Figs. 2.3 and 2.4.

Originally Nilsson used a modified harmonic oscillator potential, whereas more realistic calculations were later performed with a Woods-Saxon potential. In the Nilsson model calculated with the deformed Woods-Saxon potential, the shape of an axially symmetric nucleus is typically parametrized by parameters β_λ. In the case of a pure quadrupole deformation, the higher-order terms can be neglected and only the deformation parameter β is required for parameterization. It is connected to the eccentricity of an ellipse via the relation

$$\beta = \frac{4}{3}\sqrt{\frac{\pi}{5}}\frac{\Delta R}{R_{\text{ave}}},$$ (2.1)

where $\Delta R = a - b$ is the difference between the semi-major and semi-minor axes of the axially symmetric nuclear ellipsoid, see Fig. 2.2, and $R_{\text{ave}} \approx R_0 A^{1/3}$ is the average of the nuclear radius [29]. A value of $\beta < 0$ corresponds to an oblate shape and $\beta > 0$ to a prolate shape. The single-particle levels cross at $\beta = 0$ where they correspond to the spherical levels.

2.2.2 Geometrical model by Bohr and Mottelson

In the geometrical model developed by Bohr and Mottelson, a nucleus is described as a geometrical object and the excited states result from the collective motions of nucleons. It has three collective excitation modes, namely the spherical vibration, the axial rotation, and the non-axial rotation. The sets of collective states are called bands, in which the states are characterized with the quantum numbers K and I, where I is the total angular momentum and K is the projection of the total angular
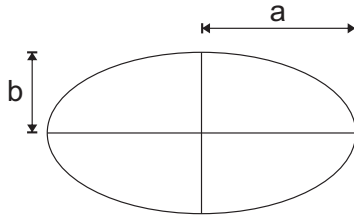
Figure 2.2: Semi-major and semi-minor axes of an ellipse.

momentum to the symmetry axis. For the rotational motion, a deformed nucleus is required. As an example, a formula for the rotational states in the $K = 1/2$ rotational band is given as

$$E_{rot} = AI(I+1) + A_1(-1)^{I+1/2}(I+1/2)\sigma(K, 1/2), \qquad (2.2)$$

where A and A_1 are the rotational constants characteristic for each rotational band. More details about the model can be found in Ref. [31]. An illustration of the positive parity levels in an axially symmetric nucleus is presented in Fig. 2.6.

2.2.3 Triaxiality and the Davydov-Filippov model

Neutron-rich nuclei around $A \approx 110$ studied in this work are typically triaxial, which means that they are axially asymmetric. The amount of asymmetry is described by the parameter γ, where $\gamma = 0°$ denote a prolate shape, $\gamma = 60°$ an oblate shape, and $0 < \gamma < 60°$ represents triaxial shapes. A convenient way to illustrate triaxial nuclear shapes are the potential energy surfaces (PES). In the PES plots the potential energy curves are plotted as a function of β and γ. Since the γ parameter defines whether the nucleus is oblate or prolate, the β parameter is usually always positive. An example of a PES calculation is given in Fig. 2.7.

Triaxial deformations are usually divided into γ-soft [34] and γ-rigid shapes [35], depending on the shape of the triaxial potential. The γ-rigid nuclei have well-defined potential minima, whereas the potential minimum for the γ-soft nucleus is wider and not so well-localized. A difference in potentials can be observed experimentally [36], since according to the Rigid Triaxial Rotor model the states in the γ-band are bunched, where $(2^+, 3^+)$, $(4^+, 5^+)$,... pairs are closer in energy. On the other hand,
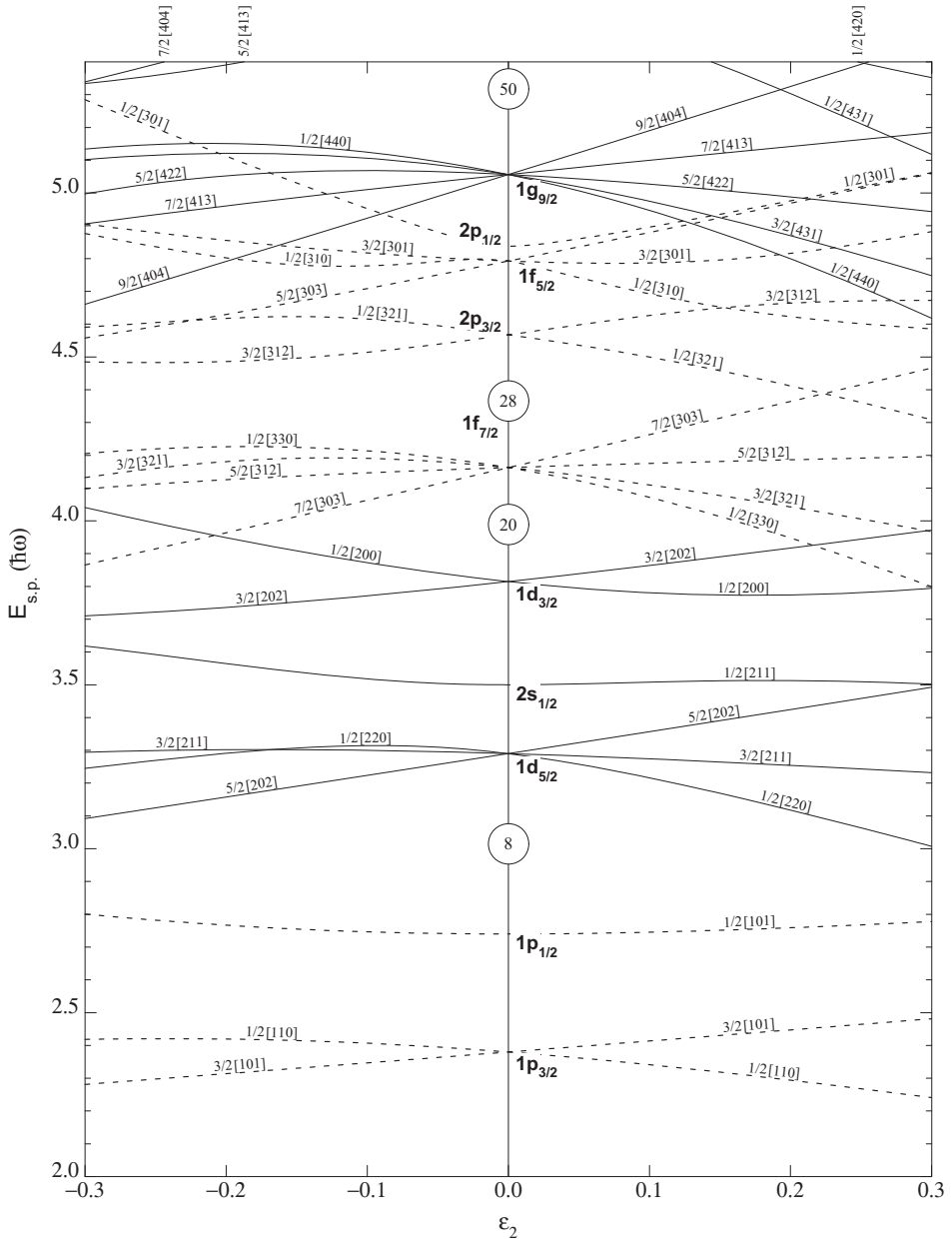
Figure 2.3: Nilsson diagram for protons and neutrons with Z or $N \leq 50$ [30]. An approximation of $\epsilon_2 \approx 0.95\beta_2$ can be used for small deformations.
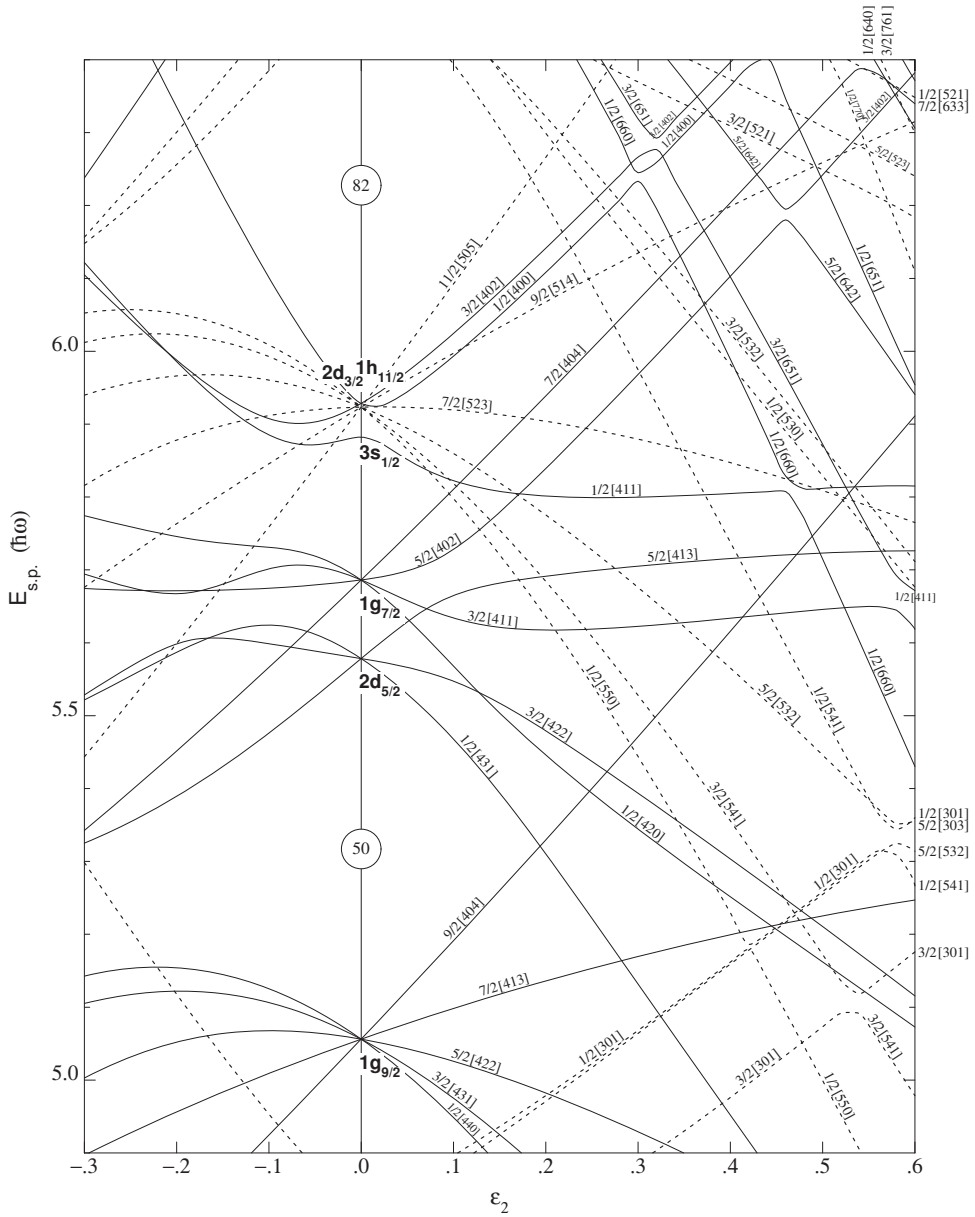
Figure 2.4: Nilsson diagram for neutrons with $50 \leq N \leq 82$ [30]. An approximation of $\epsilon_2 \approx 0.95\beta_2$ can be used for small deformations.
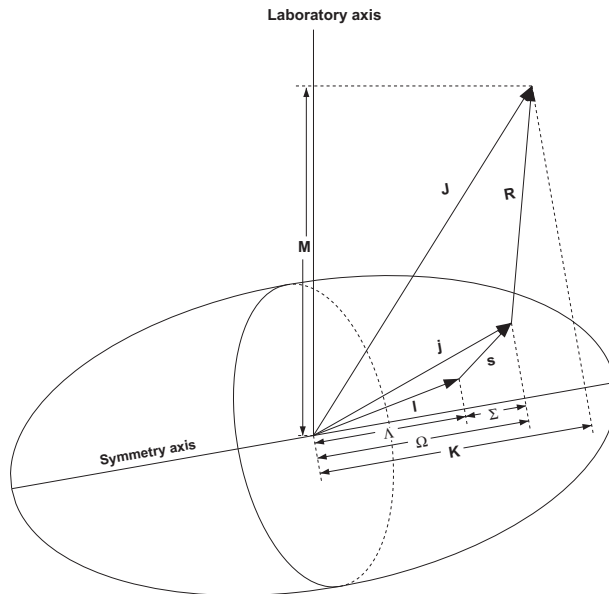
Figure 2.5: Asymptotic quantum numbers for the deformed shell model [30].
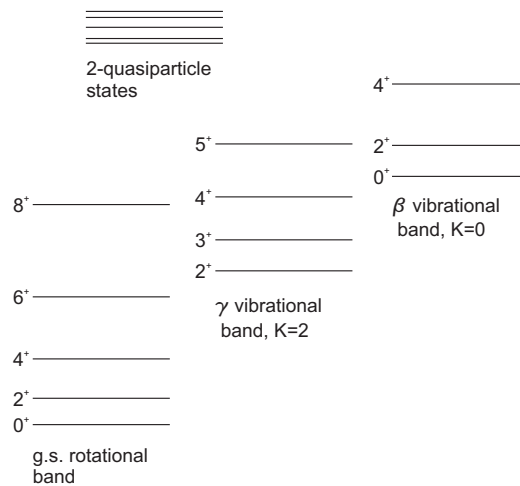
Figure 2.6: Typical positive-parity level structure of an axially deformed nucleus [32]. In triaxial nuclei the γ band is located lower in energy, see text for more details.
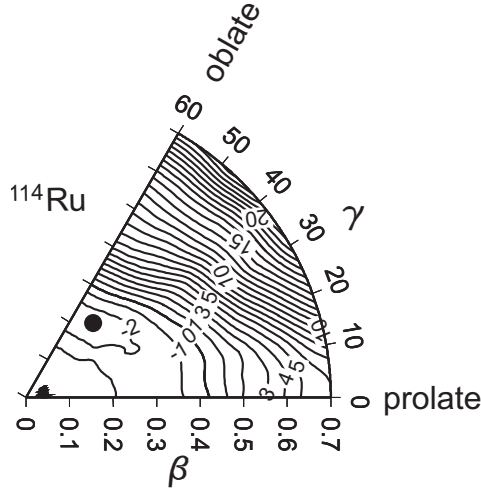
Figure 2.7: The PES surface of ^{114}Ru calculated within a microscopic Bohr-Hamiltonian approach [33] with the SIII version of the Skyrme interaction. The potential energy has its minimum at around $\beta \sim 0.23$ and $\gamma \sim 48°$ corresponding to a γ-soft oblate or "oblatish" shape.

in γ-soft nuclei, the bunching is replaced by the opposite behavior, having the pairs $(3^+,4^+)$, $(5^+,6^+)$,... closer in energy. To distinguish between these two shapes, the signature splitting function, defined as [19, 36]

$$S(I) = \frac{E(I) - E(I-1)}{E(I) - E(I-2)} \frac{I(I+1) - (I-2)(I-1)}{I(I+1) - I(I-1)} - 1 \qquad (2.3)$$

can be calculated. It is sensitive to the parameter γ giving a different staggering for γ-rigid and γ-soft deformations.

Often two empirical criteria for triaxiality in even-even nuclei have been considered, a sum rule

$$E(2_1^+) + E(2_2^+) = E(3_1^+) \qquad (2.4)$$

where $E(3_1^+)$ is the energy of the first 3^+ state, and the energy of the second 2^+ state below the first 4^+ state *i.e.* the existence of the low-lying characteristic γ band, see Fig. 2.6.

The values for the β and γ parameters can be estimated based on the energies of the collective excitations in even-even nuclei. According to Grodzins [37], the E2 transition probabilities and energies of the first 2^+ states are linked via an empirical relation [38]

$$E(2^+) \cdot B(E2; 2_1^+ \rightarrow 0_1^+) \approx 2.5 \cdot 10^{-3} Z^2 A^{-1} [\text{MeV } e^2\text{b}^2]. \tag{2.5}$$

From equation (2.5) one can derive an approximate relation for the β parameter for axially symmetric nuclei [38]

$$\beta^2 \approx \frac{1224}{E(2^+)A^{7/3}} \text{MeV}, \tag{2.6}$$

where A is the mass number and $E(2^+)$ is the energy of the first 2^+ state [39]. In triaxial nuclei, the β value given by equation (2.6) has to be corrected with a factor [38]

$$\beta_\gamma = \beta \left(\frac{9 - \sqrt{81 - 72 \sin^2(3\gamma)}}{4 \sin^2(3\gamma)} \right)^{1/2}. \tag{2.7}$$

A theory of Davydov and Filippov [35,38] provides an estimate for the γ parameter based on the ratio of the first two 2^+ states in even-even nuclei

$$\gamma = \frac{1}{3}\sin^{-1}\left[\frac{9}{8} \left(1 - \left(\frac{R_\gamma - 1}{R_\gamma + 1} \right)^2 \right) \right]^{1/2}, \tag{2.8}$$

where $R_\gamma = E(2_2^+)/E(2_1^+)$ and the $E(2_1^+)$ and $E(2_2^+)$ are the energies of the first and second 2^+ states, respectively. The γ parameter can be calculated also from the reduced E2 transition probabilities. The required equations can be found in Ref. [35].

2.2.4 Interacting boson model

The interacting boson model (IBM) or interacting boson approximation (IBA) are nuclear models which have some features common with the nuclear shell model

(γ unstable)

O(6)

Ru, Pd   Pt, Os

SU(5)   SU(3)
(vibrational)   Sm, Nd   (rotational)
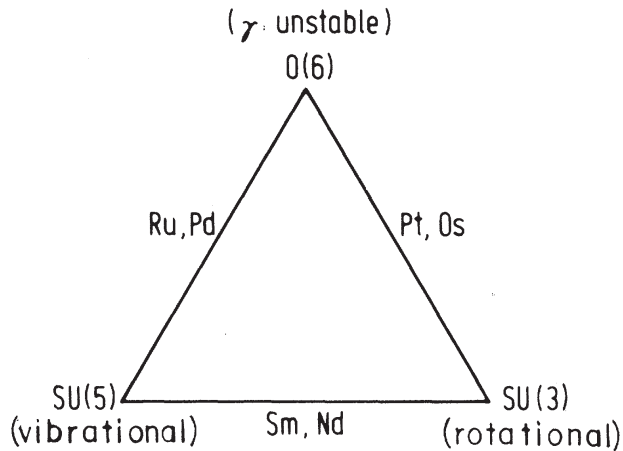
Figure 2.8: A symmetry triangle of the IBA-1 model illustrating the three limiting symmetries corresponding to the SU(5) (vibrational), SU(3) (rotational), and O(6) (γ unstable) limits [41].

and the geometrical model by Bohr and Mottelson. The IBA model describes the nucleon pairs as bosons with angular momenta $l = 0$ or 2 corresponding to the s and d bosons, reducing remarkably the number of single-particle states given by the shell model. The model has three limiting symmetries, SU(5), SU(3), and O(6), which have the vibrational, rotational (axial) and γ unstable as geometrical model analogs, respectively. With the IBA model one can also calculate the properties of the transitional nuclei between the three limits. In Fig. 2.8 a symbolic triangular representation of the model is presented. The IBA model is discussed in more detail in Ref. [40].

The three different symmetries can be experimentally identified in even-even nuclei by investigating the $\frac{E(4^+)}{E(2^+)}$ ratio. It has the value of 2 for the spherical vibrational nuclei, increasing as a function of deformation, reaching the maximum value of 3.3 corresponding to the rigid axial rotor. A value of a γ unstable rotor is 2.5 [41]. Also useful predictions for $B(\text{E2})$ ratios have been calculated with the IBA model, see Ref. [41].

2.3 Nuclear decay

Independent of the type of radioactivity, in a nuclear decay process a nucleus transforms into another by emitting one or more particles. The amount of a certain radioactive species as a function of time is described by a radioactive decay law

$$N(t) = N_0 e^{-\lambda t} = N_0 e^{\frac{-\ln 2 \cdot t}{t_{1/2}}}, \tag{2.9}$$

where N_0 is the number of radioactive atoms at time $t = 0$ and λ is the decay constant or the decay probability per unit time, which is inversely proportional to the half-life $t_{1/2}$. The number of radioactive daughters as a function of time is

$$N(t) = N_0 \frac{\lambda_1}{\lambda_2 - \lambda_1} e^{-\lambda_1 t} - e^{-\lambda_2 t}, \tag{2.10}$$

where λ_1 and λ_2 are the decay constants of the first and second decaying species. These are the two simplest cases of the so-called Batemans equations [42,43] describing the nuclear concentrations after a time t. For the longer decay chains, a general form of the Batemans equation reads

$$N_n(t) = \frac{N_1(0)}{\lambda_n} \sum_{i=1}^{n} \lambda_i \alpha_i e^{-\lambda_i t}, \tag{2.11}$$

where

$$\alpha_i = \prod_{j=1, j \neq i}^{n} \frac{\lambda_j}{\lambda_j - \lambda_i}. \tag{2.12}$$

The activity is defined as the number of decays per time unit

$$A = -\frac{dN}{dt} = \lambda N. \tag{2.13}$$

Since the activity is usually experimentally detected rather than the number of particles, it is a more important quantity from the experimentalists point of view.

2.3.1 Beta decay

The nuclear beta decay is a weak interaction process between two neighboring nuclear isobars. It can be divided into three types: β^-, β^+ and electron capture. On the neutron-rich side of the nuclide chart, only the β^- decay is possible and therefore the discussion here is restricted only to this mode. In the β^- decay, a neutron is converted to a proton, and an electron and its antineutrino are emitted. The underlying process is a conversion of an up quark into a down quark by a W^- boson exchange. The available decay energy, defined as the mass difference between the mother and daughter nuclei, is called a decay Q value. In many cases the daughter nucleus is left in an excited state, which decreases the total kinetic energy by the amount of the excitation energy of the state. This value sets the available kinetic energy for the final state divided between the three final particles (nucleus, e^- and $\bar{\nu}$), although the recoil energy of the nucleus is small compared to the kinetic energy of the electron. Because the beta decay is a three body process, the energy spectrum of the electron is a broad distribution instead of a sharp peak.

The beta decay can be divided into two types depending on the angular momentum carried by the emitted particles. In Fermi decay the spins of the electron and its antineutrino are antiparallel and in Gamow-Teller decay they are parallel. These can be further divided into so-called allowed and forbidden transitions depending on the angular momentum carried by the leptons. The selection rules for different types of transitions are presented in Table 2.1.

As a general rule, the beta decay rate is proportional to the fifth power of the transition energy. Therefore, it is convenient to compare the decay probabilities using logarithms of so-called comparative half-life (ft) values, defined as

$$ft = \frac{C}{\langle M_F \rangle^2 + (\frac{G_A}{G_V})^2 \langle M_{GT} \rangle^2},\tag{2.14}$$

where f is a phase space factor containing the energy dependence and t is a partial half-life for the given state. The $\langle M_F \rangle$ and $\langle M_{GT} \rangle$ are the Fermi and Gamow-Teller matrix elements, $\frac{G_A}{G_V}$ is the ratio of the axial vector and vector coupling constants and C is a constant. The numerical values of the constants are $\left| \frac{G_A}{G_V} \right| = 1.2695(29)$ [44] and $C = 6147.0(24)$ s [45]. Typical log ft values for the beta transitions of different types are presented in table 2.1.

When comparing the beta-decay probabilities to different levels in the daughter

Table 2.1: Beta decay selection rules and typical log ft values [49,50]. Transitions which are not possible if either I_i or I_f is zero are given in parenthesis.

Transition type	L	ΔI (Fermi)	ΔI (Gamow-Teller)	$\Delta\pi$	Log ft
Allowed	0	0	0,1	No	3.8-6.0
1st forbidden	1	(0),1	0,1,2	Yes	6-10
2nd forbidden	2	(1),2	2,3	No	11-13
3rd forbidden	3	(2),3	3,4	Yes	17-19
4th forbidden	4	(3),4	4,5	No	> 22

nucleus, in addition to log fts, the Gamow-Teller strengths can be used. For the pure GT decay the strength is defined as

$$B(GT) = \frac{1}{ft} \frac{C}{\left(\frac{G_A}{G_V}\right)^2}.$$

(2.15)

The total GT strength is defined as the sum of all individual transition strengths

$$B_\Sigma(GT) = \Sigma B_i(GT).$$

(2.16)

In the case of deformed nuclei, the beta decay obeys additional asymptotic quantum number selection rules. In the case of $\Delta\Omega = 1, \Delta N = \Delta n_z = \Delta\Lambda = 0$, the beta transition is called allowed-unhindered (au). Such kind of transitions can be identified by their low log ft values (log $ft \leq 5$). If $\Delta\Omega = 1, \Delta N = 0, |\Delta n_z| = |\Delta\Lambda| = 0$ or ± 1, the beta-decay is called allowed-fast, being relatively fast, though slower than the au transitions. All other allowed transitions violating the asymptotic quantum number selection rules are called allowed-hindered [46, 47].

In addition, the beta transitions can be hindered due to nuclear structure effects. Such transitions are, for example, isospin-forbidden (between $I{=}0$ states of different isospin *i.e.* non-analog states), l-forbidden ($\Delta l > \Delta I$, log $ft \geq 5.0$) and K-forbidden ($\Delta K > \Delta I$) [48] transitions.
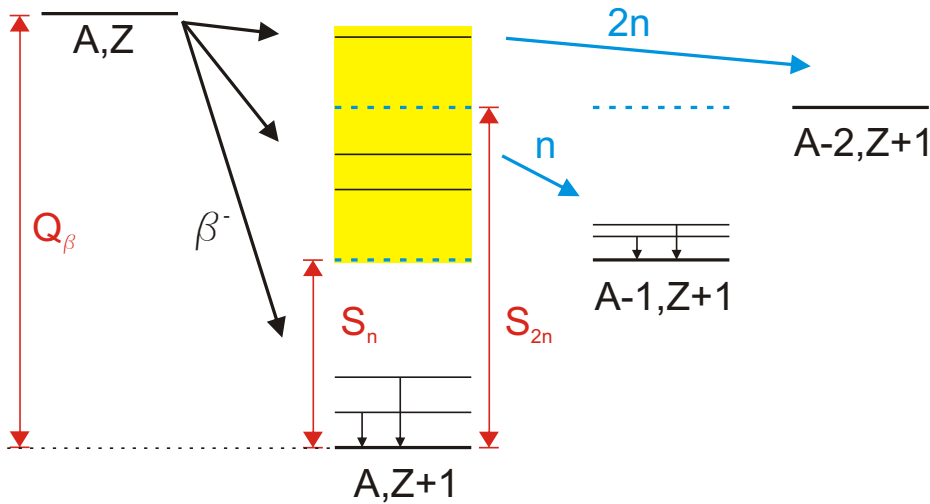
Figure 2.9: A beta-delayed neutron emission process.

2.3.2 Beta-delayed neutron emission

A beta-delayed neutron emission is a process whereby a neutron-unbound excited state is populated by the beta transition from a neutron-rich precursor nucleus followed by the emission of a neutron. It becomes energetically possible when the beta decay Q value is greater than the one neutron separation energy

$$Q_\beta > S_n. \tag{2.17}$$

Also a two-neutron emission is possible if

$$Q_\beta > S_{2n}, \tag{2.18}$$

where S_{2n} is the separation energy of two neutrons. When moving away from the line of beta stability, the Q_β values typically get larger and S_n values get smaller. Thus as this energy window increases, so does the probability of neutron emission. Consequently, the beta-delayed neutron emission is regularly observed far from beta stability. The beta-delayed neutron emission process is illustrated in Fig. 2.9.

Above the nucleon separation energy (S_n for neutrons) the nucleons are bound by the Coulomb potential and the centrifugal potential. Unlike the protons, the neutrons are bound only by the centrifugal potential

$$V_l(r) = \frac{l(l+1) \cdot \hbar^2}{2 \cdot \mu \cdot r^2},$$ (2.19)

where l is the orbital angular momentum of the neutron and μ is the reduced mass, defined as

$$\mu = \frac{m_n \cdot M_{A-1}}{m_n + M_{A-1}},$$ (2.20)

where M_{A-1} is the mass of the daughter nucleus. In the case of $l = 0$ the centrifugal potential is zero and consequently the $l = 0$ neutron emission ($|J_{\text{emitter}} - J_{\text{daughter}}| = 1/2$) is more probable compared to the higher l neutron emissions. Therefore, the spin of the decaying state in the precursor nucleus can be estimated from the population pattern in the daughter nucleus [51]. Since the lifetime of the excited level in the emitter nucleus is much shorter compared to the beta-decay half-life of the precursor, one can define the half-life of the precursor nucleus from the beta-delayed neutrons. In addition, the measured P_n values can give information about the beta strength distribution above the S_n.

2.3.3 Electromagnetic transitions

In many cases the radioactive decays such as beta decay leave the daughter nucleus in an excited state, which usually de-excites by an electromagnetic transition. These transitions are divided into gamma and conversion electron transitions where, in the former case, a gamma ray is emitted and in the latter case one of the atomic electrons is emitted followed by the emission of Auger electrons or X rays due to a vacancy created in an atomic shell.

Long-lived excited states with measurable half-lives are called isomers or isomeric states. These states can decay also by other decay modes, such as beta decay. Due to the development of experimental methods, nowadays the definition of an isomer is used for states with lifetimes shorter than in previous times. A typical limit for a half-life of the isomer is 1 ns [52].

Gamma decay

The gamma transition probability between the initial and final states with angular momenta I_i and I_f, respectively, is given by the following formula:

$$\lambda(L) = \frac{1}{\tau} = \frac{8\pi(L+1)}{\hbar L[(2L+1)!!]^2}\left(\frac{E_\gamma}{\hbar c}\right)^{2L+1}B(ML; I_i \rightarrow I_f),\qquad(2.21)$$

where τ is the mean lifetime of the state, $B(ML; I_i \rightarrow I_f)$ is the reduced transition probability, E_γ is the energy difference between the states in MeV, M defines the character of the transition (E for electric and M for magnetic transitions) and L is the index of radiation. According to the conservation law, L can have values of

$$|I_i - I_f| \leq L \leq |I_i + I_f|.\qquad(2.22)$$

The multipole order of the transition is defined as 2^L ($L{=}0$ for monopole, $L{=}1$ for dipole, $L{=}2$ for quadrupole etc). In gamma decay monopole transitions are not allowed and they can proceed only via internal conversion or internal pair production. The parity selection rule for gamma transitions is

$$\pi_i \pi_f = \begin{cases} (-1)^L & \text{for } EL \\ (-1)^{L+1} & \text{for } ML. \end{cases}\qquad(2.23)$$

Internal conversion

Internal conversion is a process competing with the gamma-ray emission. In this process the nuclear transition energy is transferred to one of the atomic electrons causing the emission of the electron. The kinetic energy of the emitted electron is defined as

$$T_e = (E_f - E_i) - B_n,\qquad(2.24)$$

where $(E_f - E_i)$ is the energy difference between the initial and final states of the nucleus and B_n is the atomic binding energy of the emitted electron. The ratio between the internal conversion and gamma transition probabilities defines the total internal conversion coefficient (α or ICC) of the transition:

$$\alpha = \frac{\lambda_e}{\lambda_\gamma}. \tag{2.25}$$

The total transition probability is defined as

$$\lambda = (1 + \alpha)\lambda_\gamma, \tag{2.26}$$

where α is the sum of the contributions from different atomic shells. The emission of an electron creates a vacancy in an atomic shell, which is filled by an electron from an outer shell. The excess energy can be again released by electromagnetic radiation (X-ray emission or by an atomic electron emission). The kinetic energy of the second electron, called the Auger electron is defined as

$$T = B_V - B_F - B_E, \tag{2.27}$$

where B_V is the binding energy of the shell with an initial vacancy, B_F is the binding energy of the outer shell electron, which moves to fill the vacancy and B_E is the binding energy of the emitted Auger electron. This process creates two new vacancies in the atomic shells, which again are filled leading to Auger-electron or X-ray emissions. A cascade of Auger electrons leaves the atom highly charged.

The charge state of an atom is increased also due to a shake-off electron emission. In this process, the atom has to rearrange its atomic shells due to a change in the central potential caused by the nuclear decay. Therefore, some electrons may be excited to higher atomic shells (shakeup) or may be emitted (shake-off) [53–56]. The shakeup electrons cause a loss in the energy of the conversion electron and the shake-off electrons show up as a continua close to zero energy and complementary shake-off satellites near the conversion energy peak. More information about atomic shell effects in nuclear decay can be found in Ref. [57]. An estimate for the charge state of the atom as the result of the sudden inner-shell vacancy can be found in Ref. [58].

Since the internal conversion probability depends on the multipolarity and on the character of the gamma transition, it can be used as a tool to define the transition multipolarities. If the spin of either the initial or the final state of the electromagnetic transition is known, the other can be defined from the multipolarity of the transition. In this work, a so-called X-ray method has been used to estimate the multipolarities. In this method the ratio of the number of X rays and the intensities

of the gamma rays in coincidence with a particular gamma transition corrected with the fluorescence yield (ω = a probability for the X-ray emission) defines the conversion coefficient of that transition. The experimentally defined conversion coefficient can be compared to theoretical values [59] and the multipolarity of the transition can be defined. To be reliable, this method requires a quite a simple and well-known decay scheme.

2.4 Interpretation of the structure

2.4.1 Odd-odd nuclei and the parabolic rule

In a simplified picture the low-energy levels in an odd-odd nucleus can be described by coupling the odd-proton levels to the odd-neutron levels. As a first estimate, both can be taken from the neighboring nuclei. In the case that the low-lying levels are of single-particle nature, the level sequence of odd-odd nuclei can be predicted by using a so-called parabolic rule invented by Paar [60]. The odd proton and neutron form multiplets by coupling the spins of each particle j_p and j_n to I. The energy levels $E(I)$ lie on a parabola versus $I(I+1)$. The parabola is open downwards if the proton and neutron levels have the same character *i.e.* both are either particle or hole states. If the parabola is open upwards, the characters or the particles are different. In the case of a downward-opening parabola, the lowest level has either the lowest or highest spin I and it has a chance to form an isomer due to a large spin difference between two minima. If the parabola is opening upwards, only one minimum is found and isomerism is unlikely.

Gallagher and Moszkowski [61] proposed a coupling rule for deformed nuclei:

$$\begin{cases} I = \Omega_p + \Omega_n & \text{if } \Omega_p = \Lambda_p \pm 1/2 \text{ and } \Omega_n = \Lambda_n \pm 1/2 \\ I = |\Omega_p - \Omega_n| & \text{if } \Omega_p = \Lambda_p \mp 1/2 \text{ and } \Omega_n = \Lambda_n \pm 1/2 \end{cases} . \tag{2.28}$$

In deformed odd-odd nuclei, this relation can be used to estimate whether the lowest or highest spin member of the multiplet forms the ground state. On the other hand, the remaining state has a chance to form an isomeric state.
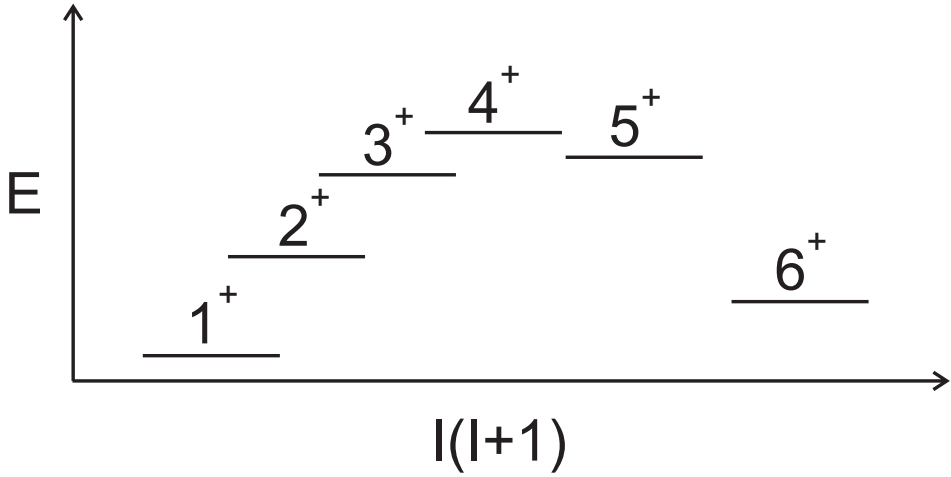
Figure 2.10: A downwards-opening parabola.

2.4.2 Alaga rules for beta and gamma transitions

Alaga rule for beta transitions

In a so-called adiabatic approximation, the nuclear wave function of an odd nucleus is a product of the even-even core and the single-particle wave function of an odd nucleon. The energy levels are organized in bands, which have the same nucleon configuration, but corresponding to the various collective rotations of the core. Therefore, the ratio of the matrix elements M_{if} between the levels of the initial beta-decaying nucleus (i) and the final states of the daughter nucleus (f), belonging to the same band, depends only on the ratio of the collective parts, which are given by the Clebsch-Gordan coefficients. For an allowed beta decay, the ratio of intensities is:

$$\frac{I(I_i, K_i \rightarrow I_f, K_f)}{I(I_i, K_i \rightarrow I'_f, K_f)} = \frac{|< I_i K_i 1 K_f - K_i | I_f K_f >|^2 \, f(Z, Q_\beta - E_{level}(f))}{|< I_i K_i 1 K_f - K_i | I'_f K_f >|^2 \, f(Z, Q_\beta - E_{level}(f))}, \quad (2.29)$$

where the quantum numbers K_i, K_f are the projections of spins I_i, I_f to the symmetry axis. The f is the phase-space factor [62] defined for the β_- decay as

$$f \approx \frac{1}{30}(E_0^5 - 10E_0^2 + 15E_0 - 6)F_0^{PR}(Z_f), \tag{2.30}$$

where $E_0 = \frac{E_i - E_f}{m_e c^2}$ and E_i, E_f are the energies of the initial and final states, respectively. F_0 is the Fermi function, written analytically by using the Primakoff-Rosen approximation [63]:

$$F_0^{PR}(Z_f) = \frac{2\pi\alpha Z_f}{1 - e^{-2\pi\alpha Z_f}}. \tag{2.31}$$

In the formula given above, α is the fine-structure constant $\alpha \approx \frac{1}{137}$ and Z_f is the proton number of the final nucleus.

Alaga rule for gamma transitions

In the case of the gamma transitions, the Alaga rule can be used to calculate the intensity ratios within one band or between the different bands. The intensity ratio given by the Alaga rule is:

$$\frac{I_\gamma(I_i, K_i \to I_f, K_f)}{I_\gamma(I_i, K_i \to I_f', K_f)} = \frac{|< I_i K_i L K_f - K_i | I_f K_f >|^2 E_\gamma(I_i - I_f)^{2L+1}}{\left|< I_i K_i L K_f - K_i | I_f' K_f >\right|^2 E_\gamma(I_i - I_f)^{2L+1}}, \tag{2.32}$$

where L is the index of radiation. One has to keep in mind that the Alaga rule is only an estimate. The bands usually mix with each other and in triaxial nuclei K is no longer a good quantum number.

3 Experimental

3.1 Production of the radioactive nuclei—the IGISOL method

In this work all studied radioactive isotopes were produced in proton- or deuteron-induced fission reactions by using the Ion Guide Isotope Separator On-Line (IGISOL) technique developed in Jyväskylä in the early 1980s [64–68]. An illustration of the technique is presented in Fig. 3.1. In this technique a thin uranium target is placed at an angle inside the light-ion fission ion guide in front of the p- or d- beam from the K130 cyclotron. The beam hits the target and the reaction products are stopped and thermalized in He gas. The charge state of the ions gradually decreases due to collisions with He atoms and impurities and finally a considerable fraction of the ions end up singly-charged.

In light-ion-induced fission reactions, the reaction products are emitted almost isotropically at an energy of around 100 MeV. Therefore, it is possible to separate the target volume by a 1 mg/cm^2-thick nickel foil, which reduces the recombination effects caused by the beam-induced plasma. The typical target thickness is 15 mg/cm^2 and it is tilted to 7° with respect to the beam axis resulting in a 120 mg/cm^2 effective thickness. Typical proton beam intensities used in experiments are of the order of 10 μA. The delay time of an ion guide is 1-100 ms, depending on the gas cell volume and the flow rate [69].

A schematic view of the IGISOL layout, as it was until June 2010, is presented in Fig. 3.2. The singly-charged ions were transported out of the gas chamber (A) by gas flow and guided through the Sextupole Ion Guide (SPIG) [70], where ion-optical properties of the secondary beam were improved. Following that the ions were accelerated forward to an energy of $30 \cdot q$ keV and mass-separated with a dipole magnet (B), having mass resolving power $R = M/\Delta M$ of the order of 300. With the electrostatic switchyard (C), the radioactive beam could be directed either to the central line for spectroscopic studies without isobaric purification or sent forward via a radio-frequency cooler/buncher (RFQ) (D) to the JYFLTRAP double Penning trap setup (E,F). The locations of the micro-channel-plate (MCP) detector and the spectroscopy setup are labeled as (G) and (H), respectively.
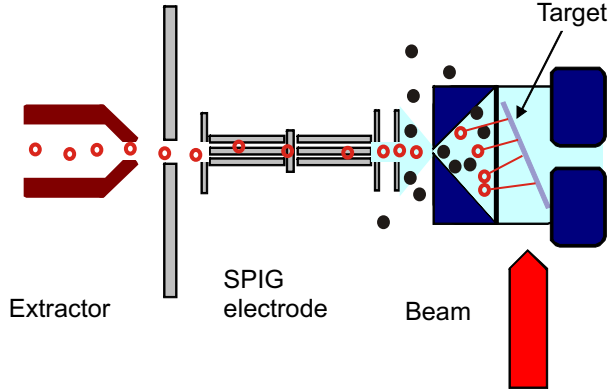
Figure 3.1: Ion guide operational principle. The open circles (red) represent the singly-
charged reaction products recoiling out of the target and the filled circles
(black) represent the buffer gas atoms and the neutralized reaction products.

The fission yields of the IGISOL facility in the A $\sim$ 110 region are reasonably high
compared to other ISOL facilities, which is mainly due to two reasons. Firstly, in
conventional ISOL facilities, such as ISOLDE [71], the reaction products are stopped
in a thick target and additional ion sources are needed to re-ionize the ions, which
can be difficult in some cases. Such cases are, for example, the refractory elements,
which come easily out from the IGISOL ion guide due to the chemical non- selectivity
of the technique. Another reason is the use of an energetic proton or deuteron beam,
in which case the mass distribution of the fission products is symmetric. This differs
from the distribution of the fission products from thermal neutron-induced fission,
which creates a more asymmetric mass distribution, having two peaks around A
= 100 and 140. The refractory elements are located between the two mass peaks,
which compensates for the low efficiency of the ion guide. The experimental total
efficiency of the method is mainly limited by the He pressure and gas cell volume,
and is of the order of 10^{-3} to 10^{-4} [72, 73].

3.2 JYFLTRAP—a triple trap setup

JYFLTRAP is an ion trap setup for purifying the IGISOL beam isobarically and for
precision mass measurements of atoms. It consists of two Penning traps inside one
superconducting 7-T magnet. In this thesis, also a radiofrequency cooler/buncher
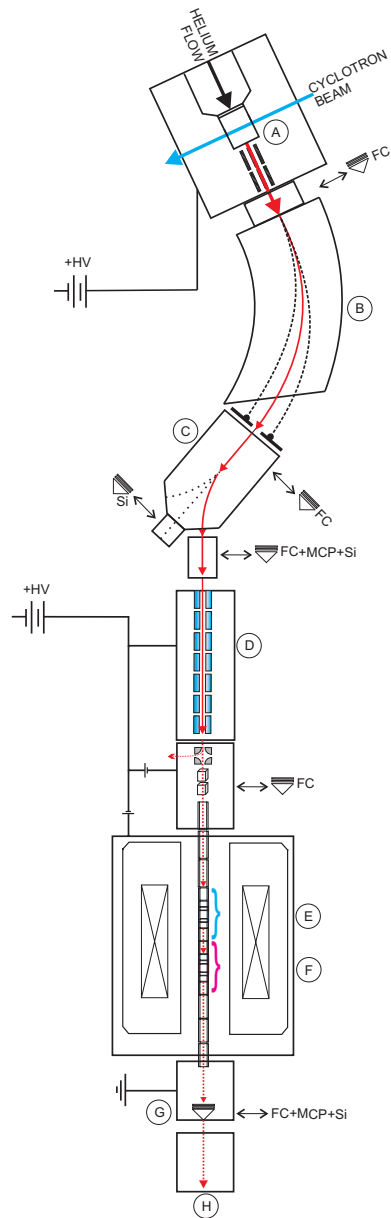
Figure 3.2: The schematic IGISOL layout before June 2010, when the move of IGISOL to the new accelerator hall was started. See text for more details.

(RFQ) [74] is considered in the JYFLTRAP setup. The first Penning trap is used for isobaric purification of the beam and it is called a purification trap [75]. The second Penning trap is called a precision trap since it is used for the precision atomic mass measurements. In some cases it can also be used to separate isomeric states [76].

3.2.1 Radiofrequency cooler and buncher

A large (> 50 eV) energy spread of the IGISOL beam has to be reduced before injecting it into the Penning trap. For this purpose a radiofrequency cooler/buncher (RFQ) has been built [74,77], which can accept quite a low-quality beam and confines it in the radial direction with an oscillating RF field. In addition, it has a segmented structure to create a voltage gradient towards the end of the device where the ions are stored before extraction. A schematic figure of the RFQ is shown in Fig. 3.3. The volume is filled with helium buffer gas with a pressure around 0.1 mbar, which is used to stop and thermalise the ions. When used in a bunched mode, the voltage of the last electrode is kept higher than the voltages of the other electrodes, which captures the ions inside the trap. The beam of ions is extracted as bunches by lowering the voltage of the last electrode. The extracted ions are directed via a miniature RFQ to avoid recreation of the energy spread during the extraction. A typical bunch width is of the order of 15 μs and the energy spread of the order of 1 eV [77]. The nominal efficiency of the device is around 60 %. The RFQ cooler is described in more detail in Refs. [74,77]

3.2.2 Operational principle of the Penning trap

A Penning trap [78] is a device which uses a superposition of a static quadrupole electric field and a strong homogeneous magnetic field to store electrically charged particles. The magnetic field confines the ions in the radial direction and the electric field in the axial direction. The magnetic field is formed at JYFLTRAP with a 7-T superconducting solenoid, which houses both traps. The electric field is formed with cylindrical electrodes, but also hyperbolical electrodes are commonly used in Penning traps, see Fig. 3.4. In cylindrical coordinates (z, r) the electric potential is of the form

$$V(z, r) = \frac{U_0}{2d^2}\left(z^2 - \frac{1}{2}r^2\right),\tag{3.1}$$
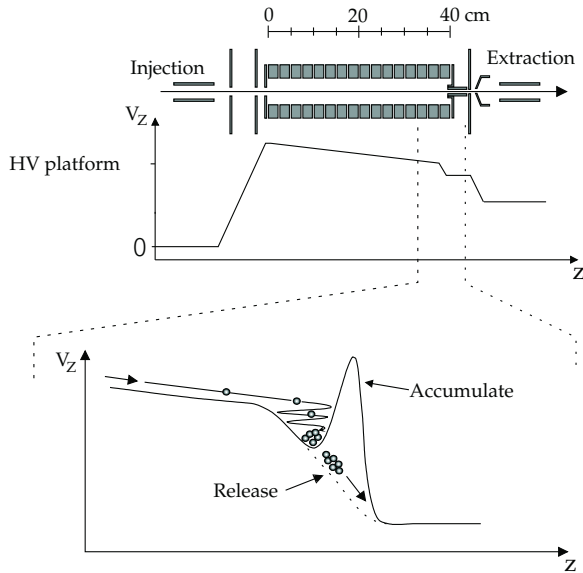
Figure 3.3: Schematic picture of the RFQ cooler/buncher. See text for more details.

where U_0 is the potential difference between the ring and the endcap electrodes and

$$d^2 = \frac{1}{2}\left(z_0^2 + \frac{r_0^2}{2}\right),$$ (3.2)

where r_0 and z_0 are the distances from the middle of the ring electrode to the inner surface of the ring and the endcap electrodes, respectively.

In a magnetic field $\vec{B}$ and an electric field $\vec{E}$, ions with an electric charge q feel a force

$$\vec{F} = m\ddot{\vec{r}} = q\left(\vec{E} + \dot{\vec{r}} \times \vec{B}\right),$$ (3.3)

where $\vec{E} = -\vec{\nabla}V$. The quadrupole electric field can be written

$$\vec{E} = \frac{U_0}{2d^2}\begin{bmatrix} x \\ y \\ -2z \end{bmatrix},$$ (3.4)
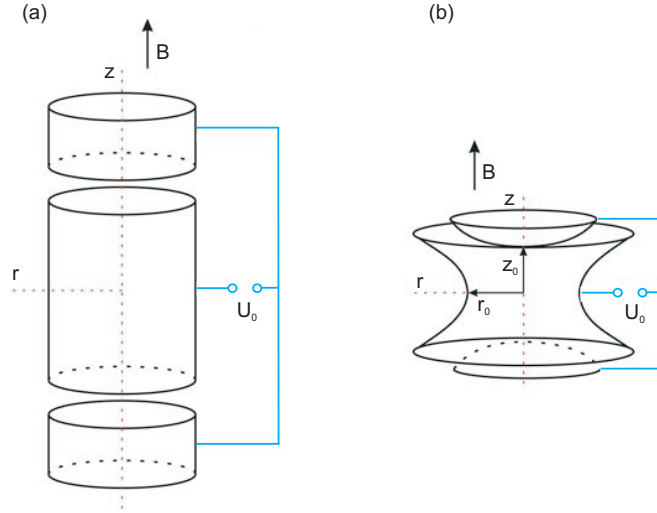
Figure 3.4: Cylindrical (a) and hyperbolical (b) electrode structures of the Penning trap. The ring electrode is the middle one and the end caps are located above and below it.

which inserted in the equation (3.3) yields

$$
\begin{bmatrix} \ddot{x} \\ \ddot{y} \\ \ddot{z} \end{bmatrix} - \frac{q}{m} B \begin{bmatrix} \dot{y} \\ -\dot{x} \\ 0 \end{bmatrix} - \frac{q}{m} \frac{U_0}{2d^2} \begin{bmatrix} x \\ y \\ -2z \end{bmatrix} = 0.
\tag{3.5}
$$

The solutions of equation (3.5) are the angular frequencies of the three eigenmotions of the trapped ions. The solution in the axial direction (z) is the angular frequency of a harmonic oscillator

$$
\omega_z = \sqrt{\frac{qU_0}{md^2}},
\tag{3.6}
$$

and the angular frequencies in the radial plane are the reduced cyclotron frequency ω_- and the magnetron frequency ω_+:

$$
\omega_\pm = \frac{1}{2} \left(\omega_c \pm \sqrt{\omega_c^2 - 2\omega_z^2} \right),
\tag{3.7}
$$

respectively. In an ideal trap, these two frequencies sum up to the true cyclotron frequency:

$$\omega_c = \omega_+ + \omega_-. \tag{3.8}$$

Typical frequencies $\nu = \frac{1}{2\pi}\omega$ of the different eigenmotions for an ion with $q = e$ and $A = 100$, are $\nu_- \approx 1$ MHz, $\nu_z \approx 100$ kHz and $\nu_+ \approx 1$ kHz. The relative magnitudes of the frequencies follow the relation

$$\nu_- \ll \nu_z \ll \nu_+ < \nu_c. \tag{3.9}$$

The eigenfrequencies ν_i are linked to the true cyclotron frequency via the invariance theorem [78, 79]

$$\omega_c^2 = \omega_+^2 + \omega_-^2 + \omega_z^2, \tag{3.10}$$

which holds even in the cases of misalignments in the axes of the electromagnetic fields.

3.2.3 Purification trap and the buffer gas cooling method

Following the beam preparation performed with the RFQ [74] the bunched beam is injected into the purification Penning trap [75]. The trap is filled with helium buffer gas with a pressure of around 10^{-4} mbar, which causes ions to lose their kinetic energy in collisions with the helium atoms. This induces damping of the fast cyclotron (ν_+) and axial (ν_z) motions and their radii decrease. On the other hand, the radius of the magnetron (ν_-) motion increases a bit. This cooling takes typically 50–200 ms.

The purification process [80] is started with a dipole excitation at the magnetron frequency, which increases the magnetron radii of all ions to a larger orbit than the 2-mm-diameter channel between the traps. To perform the excitations, *i.e.* changing the motional amplitude of the ions, the ring electrode has been split into four segments as shown in Fig. 3.5. A typical magnetron frequency in the 100-V-deep purification trap is around 1700 Hz and the typical duration of the excitation is around 10 ms with an amplitude of 300 mV.
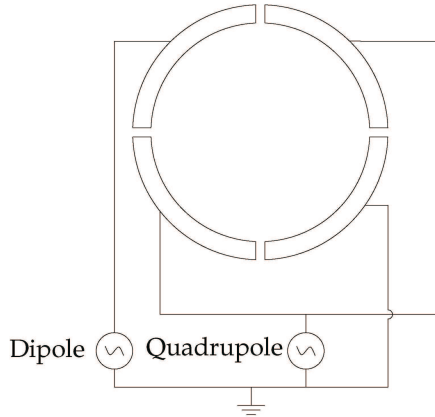
Figure 3.5: Four-fold splitted ring electrode.

A quadrupole excitation can be used to convert the two radial motions into each other. If applied in the gas-filled purification trap, the constant cooling effect of the buffer gas reduces the cyclotron motion and the ions are centered towards the trap symmetry axis. Since the quadrupole excitation is mass-selective, only the ions-of-interest are centered. Usually only one conversion of the periodic quadrupole excitation is needed. The amplitude of the excitation can be calculated from

$$V_{RF} = 2a^2 B \frac{\pi}{T_{RF}}, \tag{3.11}$$

where a is the inner diameter of the ring electrode, B is the magnetic field, and T_{RF} is the excitation time. At JYFLTRAP, one conversion occurs with [81]

$$T_{RF} V_{RF} = 11.2 \text{ mVs.} \tag{3.12}$$

The quadrupole excitation defines the transmission and the resolution of the first trap together with the buffer gas pressure and the bunch size, and therefore, the parameters of the first trap have to be a compromise between high transmission and good resolution. Generally speaking, a better resolution needs higher gas pressure and smaller bunch size as well as longer excitation time and vice versa. In mass measurements, where the transmission is not critical, longer excitation times are used if the half-life of the ion-of-interest is not a limiting factor. The best mass resolving power achieved at JYFLTRAP is around $R = M/\Delta M \approx 150000$ [82]. In

many cases, approximately three time lower mass resolving power is sufficient to purify the beam isobarically.

In spectroscopic measurements of exotic radioactive species, a better transmission is needed and shorter excitation times are used. The shorter excitations are also used to maximize the number of bunches released from the trap in a certain time unit. Typically 40 ms cooling time is applied before the excitations, 10 ms magnetron excitation, 40 ms cyclotron and 20 ms additional cooling time after the excitations are needed for a sufficient purification. Typical excitation amplitudes are around 500 mV and 300 mV for the magnetron and cyclotron excitations, respectively. An example of a purification cycle for spectroscopy measurements is shown in Fig. 3.6 and a resulting purification frequency scan is presented in Fig. 3.7.

The purified bunch of ions can be injected into the second trap for precision mass measurements or for isomeric cleaning. Another option is to direct the ions through the second trap to the spectroscopy setup located after the trap for subsequent decay spectroscopy measurements. In the case of in-trap spectroscopy, the purified bunch is kept centered in the first trap and the ions are allowed to decay in-situ. Both types of spectroscopy, in-trap and post-trap will be discussed later in more detail.

3.2.4 Precision trap for mass measurements

To perform precision mass measurements in the second trap, the time-of-flight ion-cyclotron resonance (TOF-ICR) technique [83] is used, in which the ions are again first excited to a larger magnetron radius. Following that, the ions are excited with a quadrupolar excitation which converts the magnetron motion to the reduced cyclotron motion. After the excitation, the ions are extracted and the time of flight to the microchannel plate (MCP) detector located after the trap is measured.

The ions with cyclotron motion have a radial kinetic energy $E_r(\omega_{RF})$, which induces a magnetic moment

$$\vec{\mu}(\omega_{RF}) = \frac{E_r(\omega_{RF})}{B}\hat{e}_z,$$

(3.13)

in a magnetic field $\vec{B} = B\hat{e}_z$. During the extraction, the magnetic moment of the extracted ion interacts with the magnetic field gradient $\nabla\vec{B}(z)$, which causes a longitudinal force
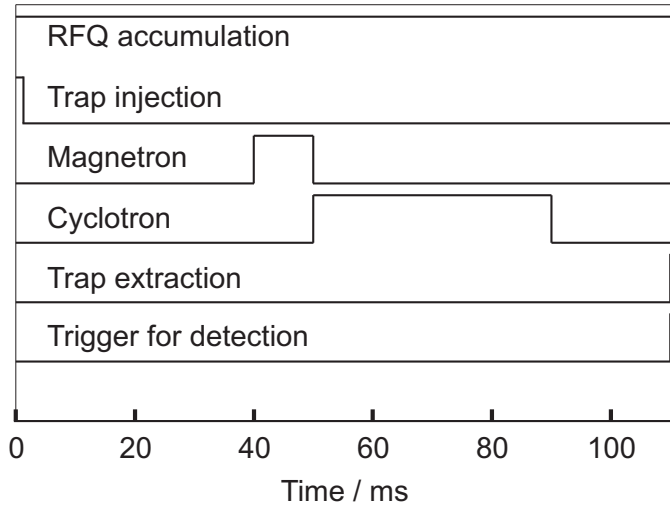
Figure 3.6: An example of the timing scheme of the purification trap. Notice the full opening of the RFQ accumulation to maximize the number of ions inside the trap, which is a common practice for measurements of exotic nuclei.
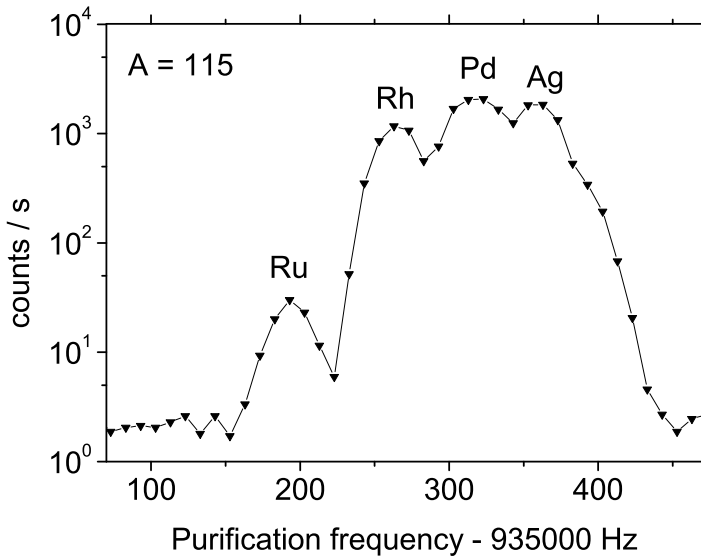
Figure 3.7: Quadrupole frequency scan of $A = 115$, where the trap has been optimized to achieve the best possible transmission for ^{115}Ru with a shortest possible purification trap cycle. The duration of the quadrupole excitation was 50 ms. In this scan a full-width half maximum ($\Delta\nu_{\mathrm{FWHM}}$) of 17 Hz was obtained, which corresponds to a mass resolving power of $R = 55000$. The obtained resolution is sufficient to separate the ^{115}Ru ions from the isobaric contaminants. The separation of the other peaks would reduce the transmission of the ^{115}Ru ions and is not needed in this case.
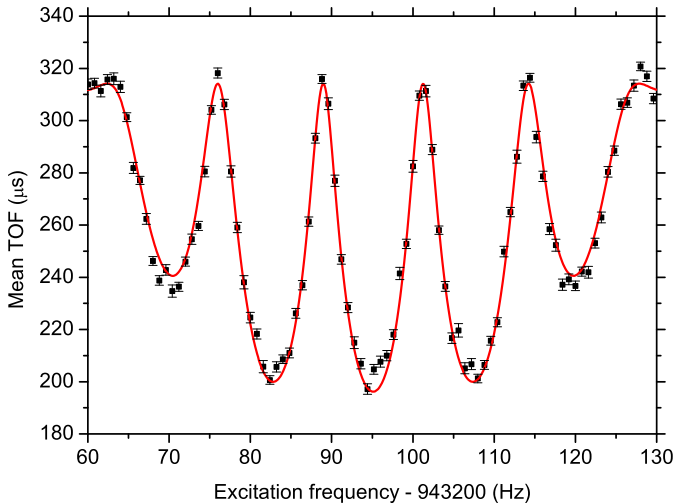
Figure 3.8: An example of the resonance curve of ^{114}Ru achieved with the Ramsey excitation scheme.

$$\vec{F}(\omega_{RF}, z) = \vec{\mu}(\omega_{RF}) \cdot \nabla \vec{B}(z). \qquad (3.14)$$

Since this force converts the radial kinetic energy into axial kinetic energy, the ions with more cyclotron motion have a shorter time-of-flight to the detector. The quadrupole excitation frequency is scanned over the resonance frequency and the time-of-flight is plotted as a function of the quadrupole frequency. The line shape from Refs. [84, 85] is fitted to the data points to obtain the exact center frequency, which corresponds to the minimum time-of-flight.

In the conventional excitation scheme, the excitation [84] is kept on over the whole excitation period. In the so-called Ramsey excitation scheme [85, 86] the excitation period has a break when the excitation is switched off between the time-separated fringes. The width of the resulting resonance is narrower for the Ramsey excitation scheme and therefore it is used in mass measurements. An example of the resonance curve achieved with the Ramsey excitation scheme is presented in Fig. 3.8.

Since the magnetic field B is not exactly constant during the measurements, it has to be calibrated with a reference ion of well-known mass. In this work only Q_β values were measured, in which case the daughter nuclide was used as a reference. The Q_β value was determined by using the equation

$$Q_\beta = M_m - M_d = \left(\frac{\nu_d}{\nu_m} - 1\right) \cdot (M_d - m_e),\qquad\qquad(3.15)$$

where m_e is the electron mass, M_m, M_d are the atomic masses, and ν_m, ν_d are the cyclotron frequencies of the singly-charged mother and daughter ions, respectively. Since the mother and daughter nuclei have the same q and A, all systematic uncertainties with the exception of short-term fluctuations in the B field are below the statistical uncertainty. The mass measurement procedure and the determination of the related uncertainties are described in more detail in Ref. [81].

3.3 In-trap conversion electron spectroscopy

In the in-trap spectroscopy technique, the radioactive ion sample is kept inside the purification trap and allowed to decay in-situ. The trapped ions can be considered as "free", since they are in practice not interacting with other ions. This feature can be utilized for spectroscopy purposes since the radiation emitted from the trapped ions does not interact with surrounding atoms. For example, conventional conversion electron spectroscopy, where the radioactive ions are implanted into a solid material, suffers from these interactions. Since a magnetic field is usually used to transport the emitted electrons efficiently to the detector, the electrons which have scattered inside the source material have also been transported to the detector. The scattered electrons have lost energy inside the source, which can be seen in the resulting spectrum as a distorted line shape or as a low-energy tail of the full-energy peak. This kind of asymmetric line shape makes the precise definition of the centroid energy and the area of the peak challenging [87]. A comparison between the conventional conversion electron spectroscopy and the in-trap conversion electron spectroscopy is illustrated in Fig. 3.9.

Positioning the electron detector inside the trap magnetic field allows for a very efficient electron transport to the detector. In this case one can build a setup for detecting the conversion electrons, where almost half of the electrons are transported to a single detector and the only efficiency-limiting factor is a backscattering effect, which is of the order of 20 % for silicon detectors [88, 89]. This effect is discussed in more detail in chapter 4.1.

In this work the purification Penning trap was used for a feasibility test of the in-trap conversion electron spectroscopy technique. The experimental setup is discussed in
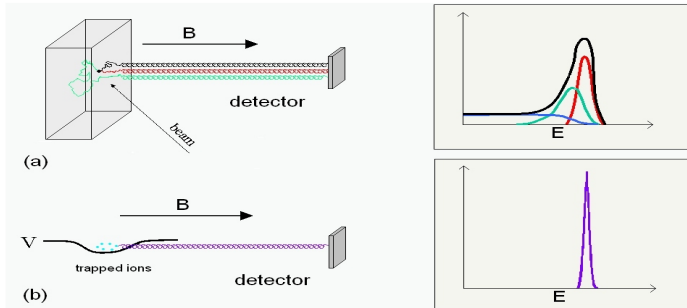
Figure 3.9: Illustration of the fundamental problem in the conversion electron spectroscopy method (a) and how it can be solved by using trapped ions as a radioactive source (b).

more detail in [Publication 1] and in Refs. [11, 90]. The main results of the work are presented in [Publication 1].

3.4 Post-trap decay spectroscopy with purified beams

A Penning trap is a useful tool for nuclear decay spectroscopy, since it can purify the roughly mass-separated IGISOL beam down to a monoisotopic level. The utilization of monoisotopic radioactive sources reduces the background level of the measured spectra remarkably. The effect of the purification is illustrated in Fig. 3.10 for $A = 115$.

For the spectroscopy measurements the detector setup was installed after the Penning trap at the end of the trap beam line. A typical setup used in this work consisted of a 2-mm-thick scintillation detector for detecting βs, a low-energy Ge detector with a thin beryllium window (LOAX) for detecting the low-energy gamma rays and X rays, and two bigger Ge detectors for detecting the high-energy gamma rays. The nominal efficiencies of these bigger detectors were around 70-80 %. The LOAX detector is the property of the University of Warsaw and the bigger Ge detectors were borrowed from the Gammapool Collaboration. The purified beam was implanted onto a movable collection tape. A schematic layout of the detector setup is shown in Fig. 3.11.
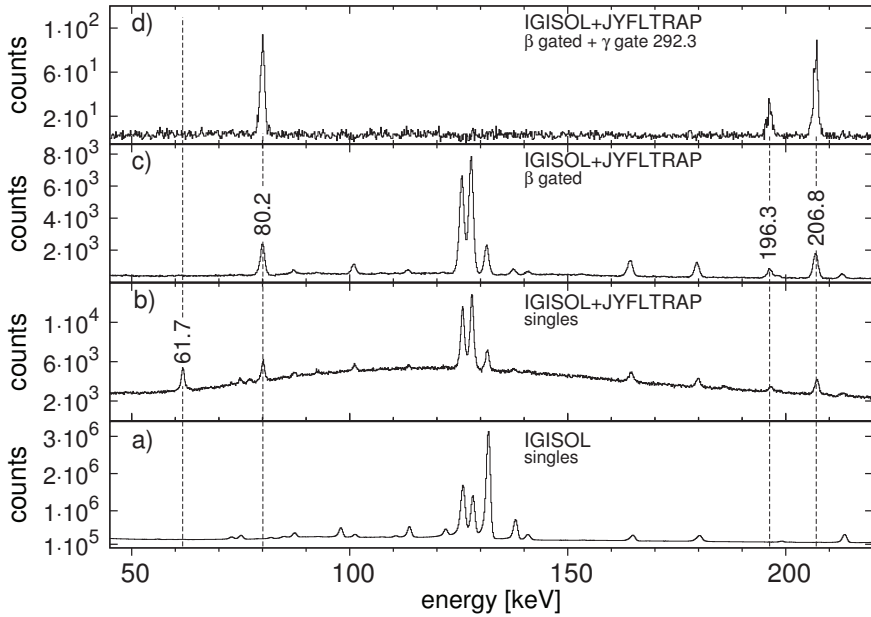
Figure 3.10: Gamma-ray spectra measured with a LOAX detector. (a) shows γ-rays emitted by nuclei in the A = 115 isobaric chain separated with the IGISOL only. (b) shows a singles spectrum following the beta decay of the isobarically purified ^{115}Ru samples. In (c) the spectrum of (b) is further cleaned by requiring a coincidence with βs. (d) shows the power of the purification combined with a β-γ coincidence spectroscopy setup. The gate was set on the 292.5 keV transition in ^{115}Rh. The figure is from Ref. [91].
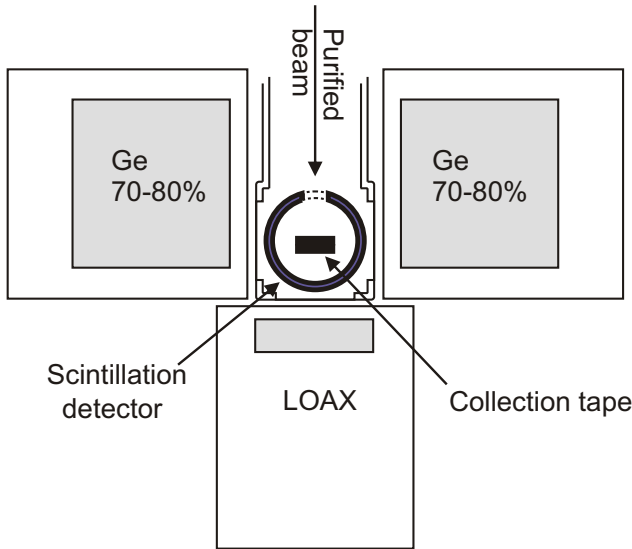
Figure 3.11: A schematic layout of the detector setup used in the decay spectroscopic studies of this work.

The data collection was performed in an event-by-event mode with the VME-based IGISOL Data Acquisition (IDA) system. Spectroscopic data was collected in the Eurogam format. The data was sorted and the coincidence relations were sought with the MIDAS software, by using the MTSort language. The level schemes of the studied nuclei were built on the basis of the $\beta - \gamma$ coincidences and the gamma intensities. The peak energies and intensities were studied by fitting a Gaussian function with the OriginPro 7.5 software [92].

3.5 Post-trap neutron spectroscopy with the BELEN-20 detector

In this work a prototype version of the BEta deLayEd Neutron detector (BELEN-20), which is being developed for the FAIR/DESPEC experiment, was connected to the JYFLTRAP beam line and tested for the first time. The utilization of the unique capabilities of the IGISOL separator coupled to the JYFLTRAP ion trap setup provides an isobarically purified radioactive sample located inside the detector setup. In addition, the chemical non-selectivity of the IGISOL technique helps to produce neutron-rich refractory elements with relatively large P_n values. Therefore,

the IGISOL facility was an excellent site for testing this kind of detector concept. Although the experiments were primarily intended for commissioning the detector for future experiments, some P_n values were also measured.

BELEN-20 detector

The BELEN-20 detector is a so-called neutron long counter detector, in which several proportional counters are mounted in a moderator matrix. The neutrons are first moderated to thermal energies, where the cross-section for absorbing a neutron is highest and following that the thermalized neutrons are converted to charged particles by using the reaction

$$^3\text{He} + \text{n} \rightarrow ^3\text{H} + \text{p} + 763.7\,\text{keV}. \tag{3.16}$$

The ionization produced by these charged particles initiates the multiplication process that leads to the detection of a neutron. Although the energy of the detected neutron cannot be extracted due to the moderating process, one can get some average energy of the neutrons by comparing the signals from the different rings, see Fig. 3.12. The advantages of using this technique are a high (30-50 %) and a rather constant detection efficiency for typical beta-delayed neutron energies ranging from 1 keV to 1 MeV. Therefore, this technique is well-suited for the P_n measurements.

The BELEN-20 detector consists of 20 ^3He counters placed inside a polyethylene matrix with dimensions of 60x60x80 cm^3. The counters are arranged in 2 concentric rings around the cylindrical beamhole of radius 5 cm. The radius of the beamhole was designed to hold a beam tube and a scintillation detector with a necessary photomultiplier as well as a typical Ge detector with a nominal efficiency of $\sim 80\%$. The beam tube contains the possibility to remove the daughter activity by using a tape transport system. The neutron background is suppressed by using the β-n and β-γ-n coincidence techniques. A schematic figure of the detector setup is presented in Fig. 3.12. The detector design was optimized via Monte Carlo simulations by using the GEANT4 [93] and MCNPX [94] codes. A triggerless data acquisition system [95] was developed and used in the experiments.
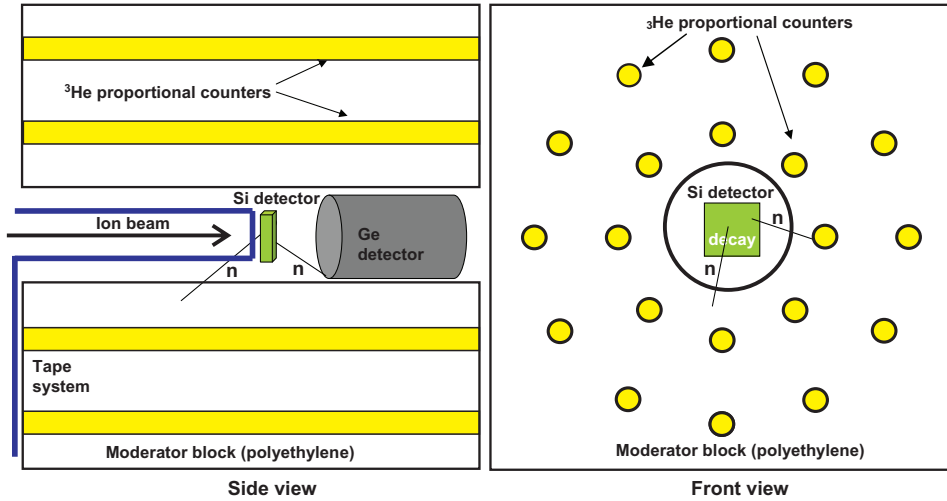
Figure 3.12: A schematic view of the detector setup, taken from Ref. [96].

Experiments at JYFLTRAP

BELEN-20 was used in two experiments connected to the JYFLTRAP beam line. The first test experiment took place in November 2009. Due to some difficulties with the size and positioning of the beam spot, the experiment was repeated in June 2010. In the first experiment, the P_n values for isotopes ^{88}Br, ^{94,95}Rb, and ^{138}I were measured and in the second, the values for ^{88,91}Br, ^{94,95}Rb, ^{137}I, ^{85,86}Ge, and ^{85}As were determined. Further details about the experiments and some preliminary results have been shown in Refs. [96, 97].

In the analysis, the following equation is used:

$$P_n = \frac{1}{\epsilon_n} \frac{N_{\beta n}}{N_\beta},$$

(3.17)

where N_β is the number of beta counts due to decay of the parent nucleus and $N_{\beta n}$ is the number of β-n-coincidences. ϵ_n is the detector efficiency for neutrons. This method is free from uncertainties in the efficiency of the beta detector. The isotopes ^{88}Br and ^{95}Rb were used as reference points when defining the detector efficiency, yielding $\epsilon_n = 27.1(8)\%$ for the detector with the moderator matrix used in the first experiment. The efficiency of the detector with a second version of the moderator

matrix is around 46 % [96].

4 Results

The main results of this work have already been published in [Publications 1-5] and will not be presented here. However, some results have been left out from the papers, which will be presented in the following chapter.

4.1 In-trap spectroscopy

In [Experiment 1] the purification Penning trap of JYFLTRAP was used for a feasibility test of the in-trap conversion electron spectroscopy technique. The measured spectra exhibit an excellent peak-to-background ratio and energy resolution as well as a very low background level, see Fig. 4.1. The results of this experiment have been presented in [Publication 1], and a short overview of the method will be given in Chapter 5. In this section issues related to the location of the silicon detector to be used for future in-trap spectroscopy experiments as well as the backscattering effect and the detection efficiency will be discussed in more detail.

4.1.1 Size of the detector

As discussed in [Publication 1], the efficiency of the in-trap detector setup was limited in [Experiment 1] by the size of the detector ($r = 1.8$ mm, see Fig. 5 in [Publication 1]). To estimate the required detector size, calculations have been performed with the SIMION 7 software [99] for three different detector locations at different magnetic fields. These calculations have been performed after the [Publication 1] to help in designing the detector setup for the future experiments.

Electrons in a magnetic field have spiraling trajectories around the field lines. If the electron detector is located after the trap electrode structure in a weaker magnetic field where the field lines have already bent away from the trap symmetry axis, the electron trajectories have also deviated further from the symmetry axis, see Fig. 4.2. Therefore, to collect all the electrons emitted from the trapped ions, the radius of the detector has to be much larger compared to the spiraling radii of the electrons.
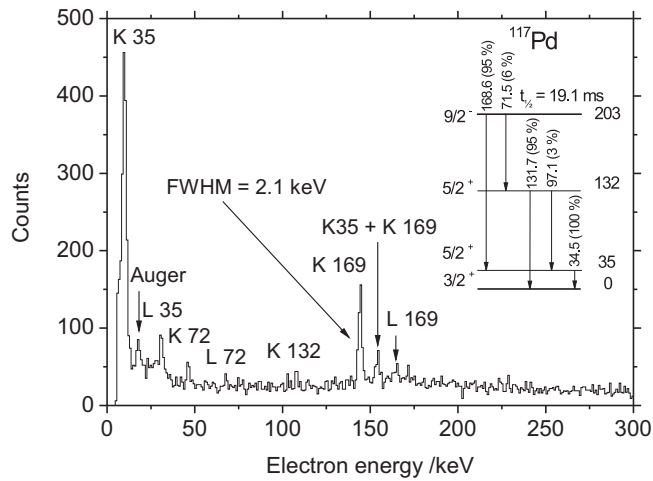
Figure 4.1: Conversion electron spectrum measured from trapped [117m]Pd ions. The background level is very low and the energy resolution is excellent (FWHM = 2.1 keV). Notice also the energy of the K conversion electron peak of the 34.8-keV transition at 9.9 keV as well as the short half-life of the decaying state ($t_{1/2} = 19.1$ ms). The partial level scheme of [117]Pd is shown in the insert [98].
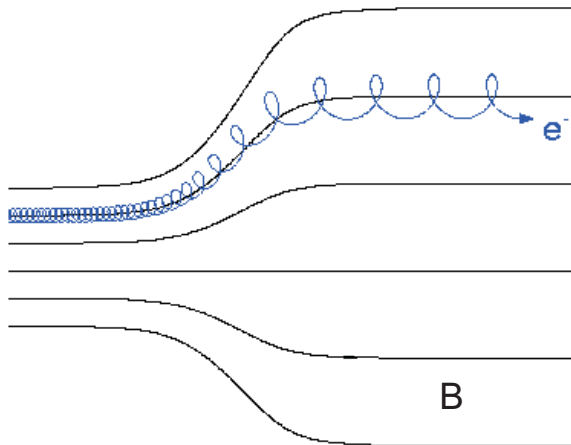
Figure 4.2: Spiraling path of an electron in a decreasing magnetic field.

The calculated size of the detector needed to collect all the electrons is presented in Fig. 4.3.

As shown in Fig. 4.3, the detector radius needed to collect all the electrons increases rapidly, when moving the detector towards the weaker magnetic field. Another feature is that if the radioactive ions are not properly centered on the trap symmetry axis, the electron trajectories deviate even further from the axis.

Another effect of the decreasing magnetic field is that the magnetic moment of an electron interacts with the magnetic field gradient, achieving a straightening of the electron track, which decreases the spiraling radius of the electron, see Fig. 4.2. This effect can be seen when comparing the solid lines showing the electron spiraling radii at a field of 0.7 T (black line) and 7 T (grey line), respectively, and the magenta data points connected with a line, where the interaction with the field gradient has been taken into account. Taking the $E = 500$ keV point as an example, the spiraling radius of an electron is $r < 0.5$ mm at 7 T (grey line), $r > 4$ mm at 0.7 T (black line) and $r \approx 2.5$ mm in the case where the electron has traveled from the 7-T magnetic field to the field of 0.7 T. The magenta points lie between the solid lines. The difference between the grey line ($B = 7$ T) and the magenta points shows how much the spiraling radius increases in the case of an electron traveling from $B = 7$ T to $B = 0.7$ T.
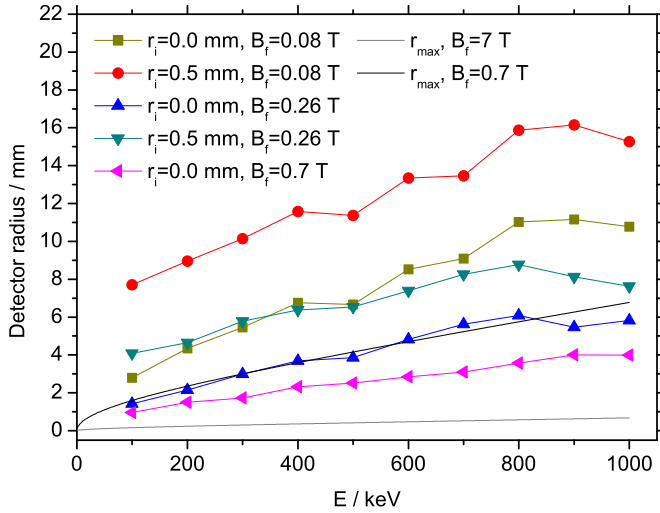
Figure 4.3: Maximal distance from the trap symmetry axis calculated for the electrons emitted from the trapped ions located at the center of the purification trap as a function of electron energy. The notation r_i represents the initial radius of the decaying ion. The different magnetic field (B_f) values correspond to the possible detector locations located at different distances from the trap center. The $B = 0.7$ T value corresponds to the location of the detector in [Experiment 1] (a distance of 535 mm from the center of the tandem trap), see Fig. 2 in [Publication 1]. The $B = 0.26$ T and $B = 0.08$ T correspond to distances 10 cm and 20 cm further away from the location of the detector in the on-line test, respectively. The solid lines show the electron spiraling radii at the field of 0.7 T (black) and 7 T (grey), respectively. See text for more details.
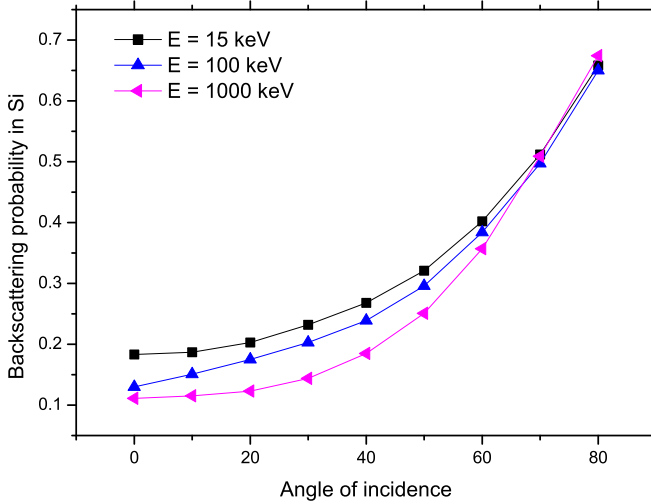
Figure 4.4: Dependence of the backscattering probability on the electron incident angle in silicon [88].

4.1.2 Backscattering effect

Conversion electrons are emitted isotropically from the trapped ions. Therefore, a fraction of the electrons are emitted at large angles with respect to the trap symmetry axis. These electrons are transported efficiently to the detector by a strong magnetic field. This could cause problems if the detector is placed in the strong magnetic field, since a large fraction of the electrons hitting the detector at large angles backscatter from the detector surface and leave only a small fraction of energy in the detector. Dependence of the backscattering probability on the electron incident angle is shown in Fig. 4.4.

Some fraction of the backscattered electrons can also reflect back to the detector due to the magnetic bottle effect. These electrons have left part of their energy in the first hit into the detector and therefore are not seen in the full energy peak. If the electrons are backscattered isotropically, approximately 5 % of the backscattered electrons can escape the magnetic bottle effect and all the electrons backscattered at a larger angle than 18° are reflected back towards the detector [90].

If the detector is located outside the trap electrode structure in a weaker magnetic field, the magnetic field gradient straightens the electron trajectories, which changes
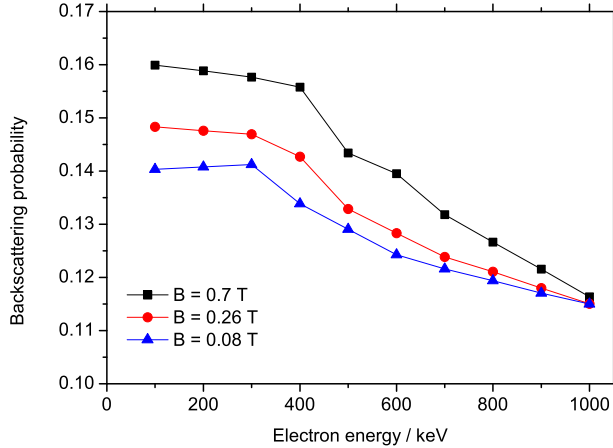
Figure 4.5: Calculated backscattering probability presented as a function of the electron energy. The magnetic field values $B = 0.7$ T, 0.26 T, and 0.08 T correspond to distances of 535 mm, 635 mm, and 735 mm from the center of the tandem trap, the first distance corresponding to the detector location in the on-line test experiment.

the incident angle of the electron towards the detector in a remarkable manner (incident angle becomes smaller than $20°$), as illustrated in Fig. 4.3. This has an effect on the backscattering probability, as presented in Fig. 4.5. At typical conversion electron energies, for example at $E = 100$ keV, the effect gained in efficiency when moving the detector 20 cm further away is of the order of 2 percent. On the other hand, moving the detector further away from the trap would require a bigger detector to collect all the electrons efficiently.

Since the size of the detector was an efficiency-limiting factor in [Experiment 1], it needs to be increased for future experiments. The size has to be optimized since the detector resolution typically gets worse in bigger silicon detectors. It has to be defined by the needed energy range, since higher-energy electrons would need a larger detector. The electron energy also defines the thickness of the detector. In addition, to perform β-ce or ce-ce coincidence measurements, a segmented detector is needed. Such a detector can also be used for the trap diagnostics, to define the size and the location of the ion bunch, for example.

Figure 4.5 shows how the backscattering effect decreases only slightly when moving the detector towards the weaker magnetic field. Therefore, the location of the

detector near to that in [Experiment 1] should be a reasonable solution for future measurements also.

4.2 ^{114}Tc beta decay

The beta decay of ^{114}Tc was studied by means of trap-assisted spectroscopy in [Experiment 3]. The Q_β value of the decay was measured and new spectroscopic data were collected. The spectroscopic data implied the existence of two beta-decaying states in ^{114}Tc, and the half-life values for both states were determined. The results related to the ^{114}Tc beta decay have been presented in [Publication 4]. In this section, the ground state spin of ^{114}Tc and the systematics of even ruthenium isotopes will be discussed in more detail.

4.2.1 Ground state spin of ^{114}Tc

In [Publication 4] the following Nilsson configurations were suggested for ^{114}Tc:

$$\pi 5/2^+[422] \otimes \nu 3/2^+[422] \tag{4.1}$$

and

$$\pi 7/2^+[413] \otimes \nu 5/2^+[413]. \tag{4.2}$$

In the former case, $\Omega_p = 5/2 = \Lambda_p + 1/2$ and $\Omega_n = 3/2 = \Lambda_n - 1/2$ and in the latter case $\Omega_p = 7/2 = \Lambda_p + 1/2$ and $\Omega_n = 5/2 = \Lambda_n - 1/2$. The rule proposed by Gallagher and Moszkowski [61] gives the ground state spin of $I = |\Omega_p - \Omega_n| = 1$ for both cases, suggesting that the 1^+ state would be the ground state and the high spin state would form an isomeric state in ^{114}Tc.

Estimates for the spins and the Nilsson configurations for odd-odd technetium isotopes can be derived by coupling the spins of the odd technetium isotopes and odd-neutron ruthenium isotopes. In the odd $^{105-113}$Tc isotopes a $(5/2^+)$ state has been observed at low energies [100], moving down and becoming the ground state spin for the $^{109-113}$Tc isotopes [100–103]. This spin assignment corresponds to the Nilsson configuration $\pi 5/2^+[422]$, see Refs. [101–103], and it can be a proton configuration for the ^{112,114}Tc isotopes as well. Since the ground state proton configuration

should not change in odd technetium isotopes, the ground state spin changes in even technetium isotopes are related to the population of the different neutron orbitals. Possible spins and Nilsson orbitals for the ruthenium and palladium isotopes have been suggested in this work, see [Publication 2] and [Publication 5] as well as section 4.4, being $1/2^+[411]$ and $3/2^+[402]$ for $N = 69$ and 71, respectively.

Ground state spins of even neutron-rich technetium isotopes are not very well known and all the suggested spin values are given in brackets in Ref. [104]. For the ^{106,108}Tc isotopes a (2^+) assignment has been suggested [105,106], and for the ^{110}Tc isotope, I = (2,3) has been proposed [107], from which the (2^+) assignment was picked by the ENSDF compiler [104]. In a recent paper a 6^- ground state and a 1^- isomeric state based on the $\nu 7/2^-[523] \otimes \pi 5/2^+[422]$ coupling has been proposed for ^{112}Tc [103].

A possible explanation for the ground state spin change in the even technetium isotopes $(2^+ \to 6^- \to 1^+)$ can follow the spin change in the odd-neutron ruthenium and palladium isotopes around $N = 70$ $(1/2^+ \to 3/2^+)$. In this case the 6^- state with a $\nu 7/2^-[523]$ configuration is an exception not seen in the odd-neutron isotopes. However, it can be easily explained by exploring the Nilsson scheme, the $\nu 7/2^-[523]$ orbital being between the $\nu 1/2^+[411]$ and $\nu 3/2^+[402]$ orbitals at moderate deformation on the oblate side of the Nilsson diagram. Possible spins and Nilsson configurations of the related isotopes are presented in Table 4.1.

The asymptotic quantum numbers $[N n_z \Lambda]$ of the alternative neutron configuration $(\nu 3/2^+[402])$ for ^{114}Tc differ from the configuration suggested in equation (4.1) and in [Publication 4], where the emphasis has been to explain the fast beta decay and allowed-unhindered pairs have been suggested. However, the $3/2^+[422]$ neutron orbital originates from the $2d_{5/2}$ spherical orbit, which is quite far away from the Fermi level in the studied region. This is illustrated in Fig. 4.6, where the Nilsson orbitals for neutrons relevant for this work are presented. The corresponding proton orbitals are presented in Fig. 4.7. A negative-parity neutron orbital, such as in ^{112}Tc, is not feasible for ^{114}Tc due to a low log ft value (4.92) of the transition to the ground state suggesting instead a fast $1^+ \to 0^+$ beta transition. Tables 4.1 and 4.2 show how the proposed Nilsson configurations for the odd-neutron ruthenium isotopes are not in conflict with the proposed Nilsson configurations for the odd-odd technetium isotopes. However, in triaxial nuclei K is not a good quantum number and the states can mix several Nilsson configurations. The Gallagher-Moszkowski rule gives a spin of 1^+ for the ground state of ^{114}Tc also with the $(\nu 3/2^+[402])$ configuration.
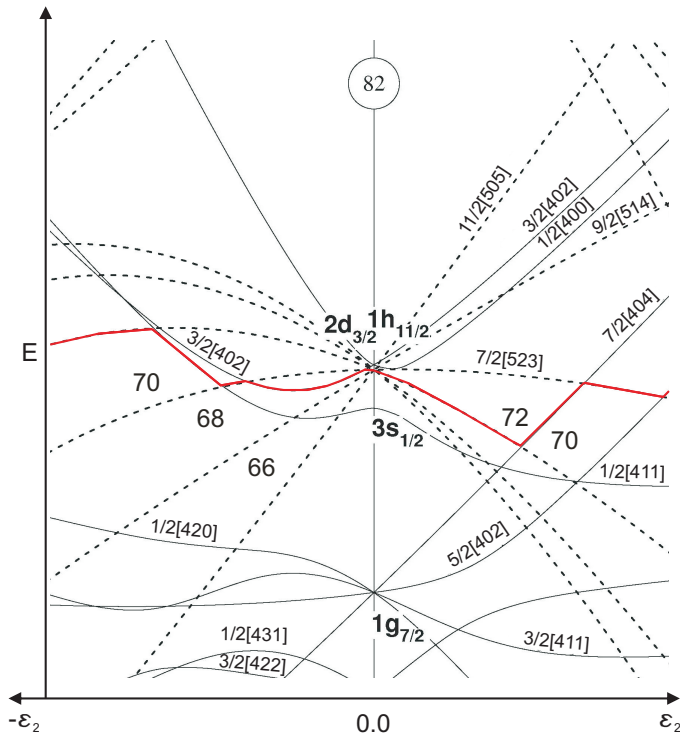
Figure 4.6: A Nilsson diagram for neutrons [30]. The red curve shows the Fermi level for $N = 70$.
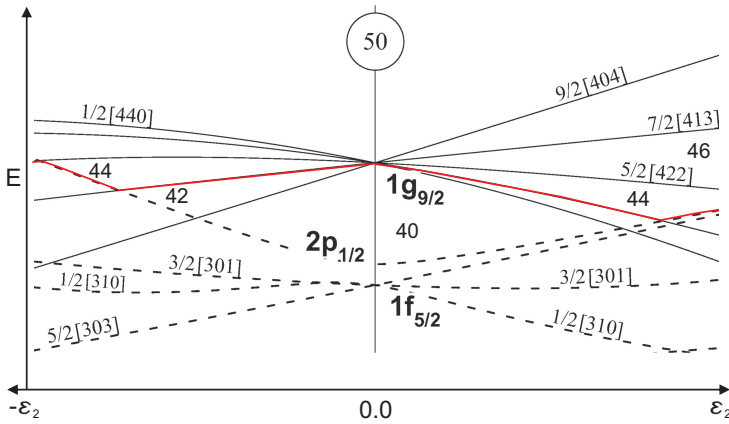
Figure 4.7: A Nilsson diagram for protons [30]. The red curve shows the Fermi level for $Z = 43$. A reader may notice that the 5/2[422] state is above the Fermi level at moderate deformation although it has been suggested to be the ground state configuration for the technetium ($Z=43$) isotopes.

Table 4.1: Possible ground states spins and Nilsson orbitals for odd-proton and odd-neutron isotopes near ^{114}Tc.

	odd Tc		odd Ru		
Isotope (Z)	I^π	orbital	Isotopes (N)	I^π	orbital
^{111}Tc (43)	$5/2^+$	5/2[422]	^{113}Ru (69)	$1/2^+$	1/2[411]
^{113}Tc (43)	$5/2^+$	5/2[422]	^{115}Ru (71)	$3/2^+$	3/2[402]

Table 4.2: Possible ground state spins and Nilsson orbitals for even technetium isotopes.

	even Tc	
Isotopes (A)	I^π	orbitals
^{110}Tc (110)	2^+	$5/2^+[422] \otimes 1/2^+[411]$
^{112}Tc (112)	1^- or 6^-	$5/2^+[422] \otimes 7/2^-[523]$
^{114}Tc (114)	1^+ or 4^+	$5/2^+[422] \otimes 3/2^+[402]$

4.2.2 Beta-delayed neutron decay of ^{114}Tc

The probability for the beta-delayed neutron emission, P_n of ^{114}Tc was measured over a decade ago at IGISOL [108], resulting in $P_n = 1.3(4)$. In this work no clear signature of the delayed neutrons was seen. A 98.5-keV gamma-ray peak was seen in the singles spectrum, which may correspond to the lowest $3/2^+ \rightarrow 1/2^+$ transition in ^{113}Ru. However, no gamma-rays were seen in coincidence with this transition and unambiguous identification cannot be made.

On the other hand, considering the 98.5-keV transition belonging to the beta-delayed neutron decay, a log ft value can be calculated. The relative intensity of the 98.5-keV transition is 3.8(7) units, which corresponds to a beta branching and P_n value of 1.4(4) for the decay of the 1^+ state and $P_n = 4.9(13)$ for the decay of the high spin state. The lower value is consistent with the earlier work. Assuming a neutron-emitting state just above the neutron separation energy ($S_n = 7058(18)$ keV [8]) of ^{114}Ru, populated by the beta decay of ^{114}Tc with the above mentioned beta branchings, the corresponding log ft values are 4.92(16) and 4.4(2) for the decays of the 1^+ and the high-spin states, respectively. These values have to be considered as lower limits, since the beta feeding can be divided between several states.

The calculated log ft values can be compared to the values reported in [Publica-

tion 4]. The log ft value for the beta-delayed neutron decay of the 1^+ state would be equal to the log $ft(1^+ \rightarrow 0^+) = 4.92(7)$ and notably smaller compared to the log ft $(1^+ \rightarrow 2_i^+) = 6.0$–6.1. The log ft value for the beta-delayed neutron decay of the high-spin state would be remarkably smaller compared to the log $ft = 5.3$-6.1 related to the high-spin decay in [Publication 4].

4.2.3 Comparison with a recent study of the high-spin states in ^{114}Ru

Very recently after the [Publication 4], an investigation of the high-spin levels of ^{114}Ru studied by measuring the prompt γ rays in the spontaneous fission of ^{252}Cf was published [117]. The results of that work are compared to the results of this work in Fig. 4.8, where the levels observed in the earlier high-spin work [109] are also shown.

The authors of Ref. [117] observed states in the ground state band (Band 1) up to spin of 14^+ and states of the one-phonon gamma band (Band 2) up to 9^+. The existence of a level at 1082.1 keV with a spin of (4^+) belonging to the gamma band, which was found in this work, was also confirmed. In addition, they found 679.5-keV and 1014.7-keV gamma-rays de-exciting the level at 1578.4 keV and also tentative 235.8-keV, 735.9-keV, and 985.0-keV gamma lines de-exciting a new level at 1813.9 keV. These levels were interpreted as members of a two-phonon gamma band (Band 3). The 1578.4-keV level was also observed in this work de-exciting via a 870.3-keV gamma line. This gamma line was not seen in Ref. [117]. The level at 2068.6 keV de-exciting via a 1360.5-keV gamma line was observed in both studies. No spin and parity assignment were given in Ref. [117] and only a lower limit for the spin (>3) was given in [Publication 4]. The experimental level energies have been compared to theoretical ones and the conclusion about triaxiality was drawn. No evidence about an oblate ground state was found.

4.2.4 Ruthenium level systematics and relation to the shape transition

Experimental observables and simple RTR and IBA models

The systematics of the lowest level energies in even ruthenium isotopes are presented in Table 4.3. One can notice how the energies of the first 2^+ states are decreasing as a function of mass number up to $A = 112$, which indicates an increase of collectivity. Then the trend starts to increase again at $A = 114$, which is also observed in the energies of the second 2^+ states. The energy ratio of the two lowest 2^+ states has the
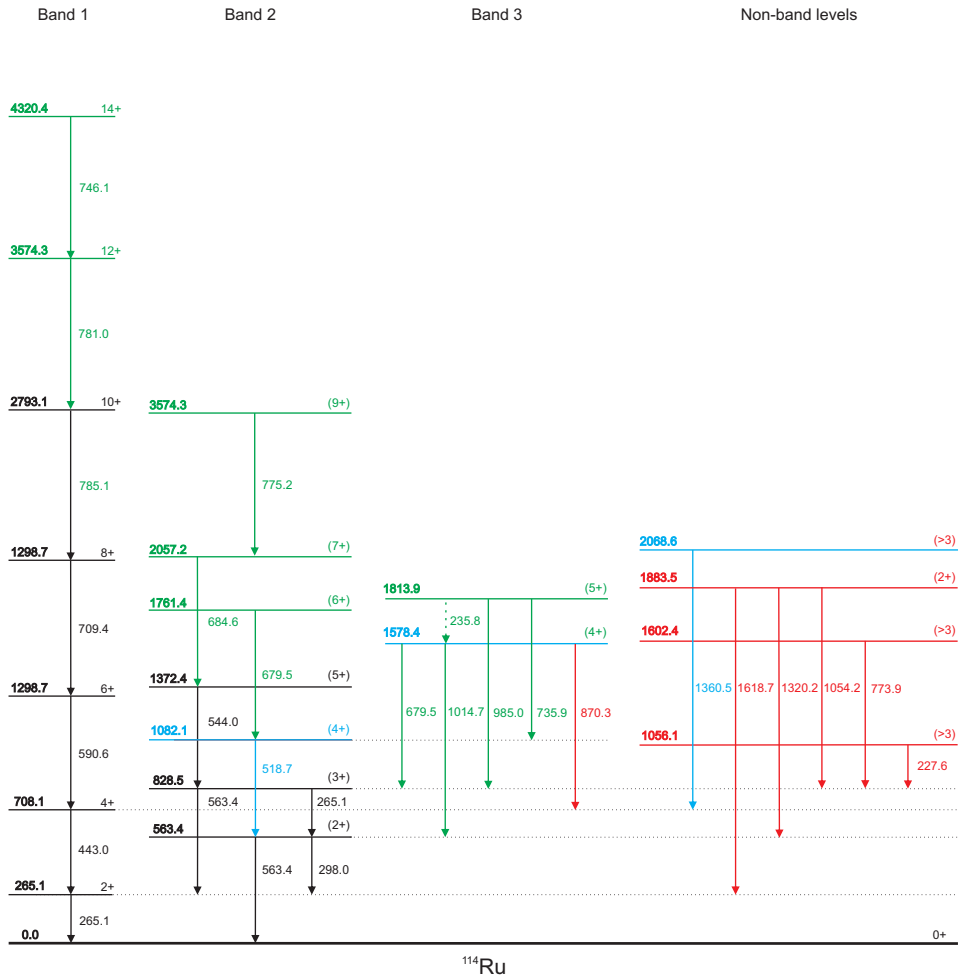
Figure 4.8: Level scheme of ^{114}Ru. The levels and gamma lines in red are from this work, in green are from Ref. [117], in blue have been seen in both studies, and in black are from Ref. [109]. See text for more details. One can observe how the prompt gamma-ray and beta-decay studies are important complementary methods to study the structure of neutron-rich nuclei.

Table 4.3: Level systematics of even ruthenium isotopes [15, 109].

Quantity	^{104}Ru	^{106}Ru	^{108}Ru	^{110}Ru	^{112}Ru	^{114}Ru
$E(2_1^+)$	358	270	242	241	237	265
$E(2_2^+)$	893	792	708	613	524	563
$\frac{E(2_2^+)}{E(2_1^+)}$	2.49	2.93	2.93	2.54	2.21	2.13
$\frac{E(4_1^+)}{E(2_1^+)}$	2.48	2.65	2.75	2.76	2.72	2.67
$\frac{E(3_1^+)}{E(2_1^+)+E(2_1^+)}$	0.99	1.03	1.03	1.01	0.98	1.00

opposite trend, increasing as a function of mass and reaching a maximum earlier at $A = 106$ and 108. The energy ratio $E(4_1^+)/E(2_1^+)$ has a similar behavior, the values starting from 2.48 at $A = 104$ reaching a maximum of 2.76 at ^{110}Ru and starting to decrease slowly when going to heavier isotopes. The values are close to the O(6) limit of the IBA model (2.5) for γ-soft nuclei.

The fifth row in Table 4.3 shows how the ratio of the first 3^+ state to the sum of two 2^+ states is close to one in all ruthenium isotopes, which is usually taken as an indication of the breaking of axial symmetry, see Section 2.2.3. In addition, the isotopes $^{110-114}$Ru fulfill a second criterion for triaxiality, having the second 2^+ state below the first 4^+ state, being a band head for a characteristic gamma band [110]. These experimental facts suggest a comparison of the experimental results with the predictions calculated from the rigid triaxial rotor model (RTR) [35]. Based on the experimental level energies and transition intensities, it was possible to extract the deformation parameter γ for ^{114}Ru from the RTR model. Three values of γ were extracted, $27.2^\circ, 27.3^\circ$, and 25.7°, the first one calculated from the energy ratio of the lowest 2^+ states and the two latter ones from the intensity ratios of $I(2_2^+ \to 2_1^+)/I(2_2^+ \to 0^+)$ and $I(3_1^+ \to 2_2^+)/I(3_1^+ \to 2_1^+)$, respectively. Since the values are similar, it indicates that our intensity ratios derived from the coincidence data are rather realistic. The γ-parameter values close to 30° suggest almost maximal triaxiality for this nuclide. The values derived from the level energies were used to calculate the ratios of reduced E2 transition probabilities B(E2) by using the RTR model [35]. The ratios for ^{110,112}Ru in addition to those derived in this work are compared with the experimental values in Table 4.4.

The theoretical values presented in Table 4.4 are not within the error bars of all

Table 4.4: Comparison of the B(E2) ratios obtained from experimental data and from the rigid triaxial rotor model calculations. Both experimental and theoretical data has been derived by assuming all transitions to be pure E2. The γ-parameter values used in the calculations are 24.2°, 26.4°, and 27.2° for ^{110}Ru, ^{112}Ru, and ^{114}Ru, respectively.

	Experiment			Theory(RTR)		
	^{110}Ru	^{112}Ru	^{114}Ru	^{110}Ru	^{112}Ru	^{114}Ru
$\frac{\text{B}(\text{E2},2_2^+\to 0_1^+)}{\text{B}(\text{E2},2_2^+\to 2_1^+)}$	0.078(8) [15]	0.036(15) [15]	0.015(6)	0.053	0.028	0.018
	0.070(7) [111]	0.040(4) [111]				
	0.067(9) [19]	0.045(7) [19]				
$\frac{\text{B}(\text{E2},3_1^+\to 2_1^+)}{\text{B}(\text{E2},3_1^+\to 2_2^+)}$	0.045^{+10}_{-8} [15]	0.013^{+33}_{-13} [15]	0.036(12)	0.065	0.025	0.015
	0.043(4) [111]	0.053(4) [111]				
	0.049(7) [19]	0.046(9) [19]				

experimental values; however, the decreasing trend is the same for both sets of ratios. In the simple RTR model, the B(E2) ratios depend only on the γ parameter, which explains the decreasing trend in theoretical ratios as the γ increases. In addition, the experimentally defined ratio $\frac{\text{B}(\text{E2},2_2^+\to 0_1^+)}{\text{B}(\text{E2},2_2^+\to 2_1^+)}$ for ^{108}Ru is 0.103 [41], which further confirms this trend.

The value of the upper ratio $\frac{\text{B}(\text{E2},2_2^+\to 0_1^+)}{\text{B}(\text{E2},2_2^+\to 2_1^+)}$ can be compared to the predictions of the IBA-1 model [41], which are 0.011 for vibrational SU(5) nuclei, 0.07 for γ-unstable O(6) nuclei and 0.7 for rotational SU(3) nuclei, respectively. The ratio $\frac{\text{B}(\text{E2},2_2^+\to 0_1^+)}{\text{B}(\text{E2},2_2^+\to 2_1^+)}$ is above the γ-soft value at $A = 106, 108$ [41] and decreasing closer to the value of the spherical vibrator yet not reaching it. However, although it is clear that the simplified IBA-1 as well as the RTR models are not the most realistic for this region, they provide us a first insight into the evolution of deformation.

The β-parameter values can be extracted from the energy of the first 2^+ state by using equations (2.6) and (2.7), which give $\beta_\gamma = 0.36$, 0.35 and 0.32 for ^{110}Ru, ^{112}Ru and ^{114}Ru, respectively. In these calculations, the same gamma parameter values have been used as in Table 4.4. The decreasing trend is similar compared to the trend in the B(E2) values, indicating a slow shape transition towards a more

spherical structure.

Potential energy surfaces calculated with modern mean-field theories

The β-parameter values for the even ruthenium isotopes presented above are slightly larger compared to the values predicted by more sophisticated theoretical calculations based on modern theories. In this work, two different approaches have been used, a Hartree-Fock-Bogoliubov (HFB) approximation with the energy density functional of Gogny-D1S type [112] and a microscopic Bohr Hamiltonian approach [113] with the SLy4 and SIII versions of the Skyrme interaction. The potential energy surface (PES) calculations with the former approach have been performed by Dr. Rayner Rodríguez-Guzmán from CSIC, Madrid and the results are presented in Fig. 4.9. The calculations with the latter methods have been performed by Dr. Leszek Próchniak from Maria Curie-Skłodowska University, Lublin and the results are presented in Figs. 4.11 and 4.12. The locations of the potential minima for ruthenium isotopes in the β-γ plane are presented in Table 4.5.

In addition to the calculated β-γ plots for the even ruthenium isotopes, the same plots have been calculated also for the even palladium isotopes with the former approach performed by Dr. Rayner Rodríguez-Guzmán. The results are presented in Fig. 4.10.

In HFB calculations the β parameter is replaced by the quadratical sum of the quadrupole operators $Q_{20} = z^2 - \frac{1}{2}(x^2 + y^2)$ and $Q_{22} = \frac{\sqrt{3}}{2}(x^2 - y^2)$:

$$Q = \sqrt{Q_{20}^2 + Q_{22}^2}. \tag{4.3}$$

The relations to β and γ are $\tan \gamma = Q_{22}/Q_{20}$ and $\beta = \sqrt{4\pi/5}Q_{20}/(A\langle r^2 \rangle)$, where A is the mass number and $\langle r^2 \rangle$ is the mean square charge radius of the nucleus [112, 114].

The potential energy surface plots presented in Figs. 4.9, 4.11, and 4.12 predict γ-soft oblate or "oblatish" shapes ($\gamma > 30°$) with a moderate deformation ($\beta \sim 0.2 - 0.25$) for $^{110-116}Ru$ isotopes. The Skyrme SLy4 interaction predicts a slightly narrower shape of the potentials compared to the SIII parametrization, see also Fig. 4.13 in the following subsection.

Some hints about the locations of the potential minima approaching to the spherical point can be found in Table 4.5, since the β values for ^{116}Ru are smaller compared

Table 4.5: Locations of the potential minima in the β-γ plane calculated with different theoretical approaches and compared with the experimental ones. $V_{\min}$ is the depth of the potential minimum relative to a spherical shape.

Method	Isotope	β	γ / $^\circ$	$V_{\min}$ / MeV
HFB	^{110}Ru	0.25	25	
HFB	^{112}Ru	0.26	30	
HFB	^{114}Ru	0.26	30	
HFB	^{116}Ru	0.18	30	
SLy4	^{110}Ru	0.23	54	-1.62
SLy4	^{112}Ru	0.23	54	-1.51
SLy4	^{114}Ru	0.25	36	-1.14
SLy4	^{116}Ru	0.0	0	0.00
SIII	^{110}Ru	0.25	36	-2.80
SIII	^{112}Ru	0.23	60	-2.79
SIII	^{114}Ru	0.23	48	-2.51
SIII	^{116}Ru	0.23	38	-1.91
Exp.	^{110}Ru	0.36	24.2	
Exp.	^{112}Ru	0.35	26.4	
Exp.	^{114}Ru	0.32	27.2	
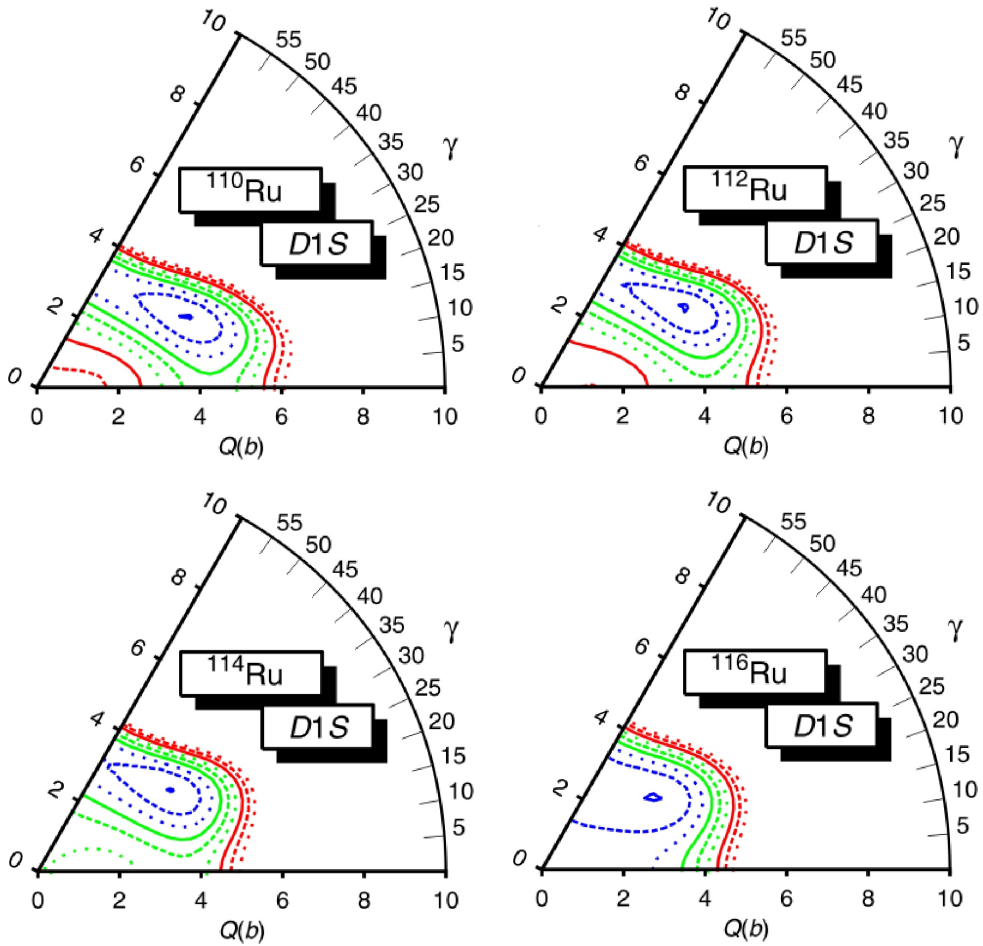
Figure 4.9: Potential energy surface plots for even ruthenium isotopes calculated with the HFB approximation with the D1S-type Gogny interaction. One can notice how these isotopes are γ-soft oblate or "oblatish". Locations of the potential minima are approaching the spherical point as N increases. These plots can be compared to the PES plots for even palladium isotopes presented in Fig. 4.10.
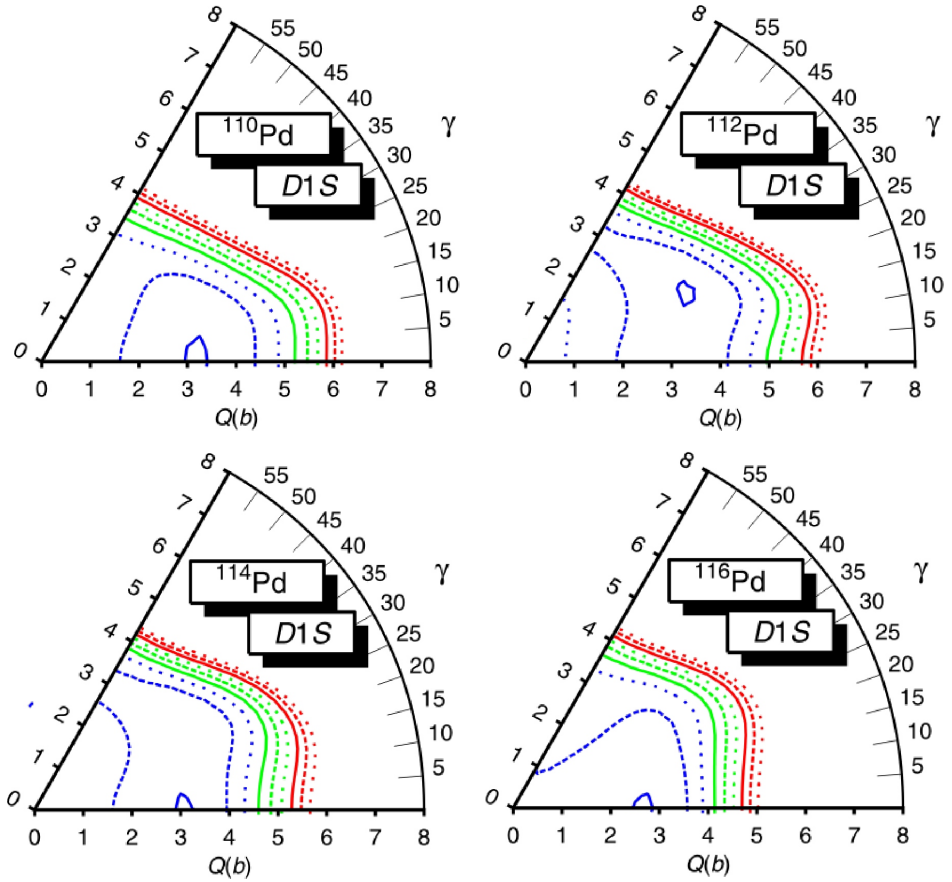
Figure 4.10: Potential energy surface plots for even palladium isotopes calculated with the HFB approximation with the D1S-type Gogny interaction. These isotopes exhibit weak and relatively soft prolate shapes and therefore differ from the ruthenium isotopes, which have γ-soft oblate shapes, see Fig. 4.9.

Figure 4.11: Potential energy surface plots for even ruthenium isotopes calculated with the microscopic Bohr-Hamiltonian approach with the SLy4 type of Skyrme interaction.
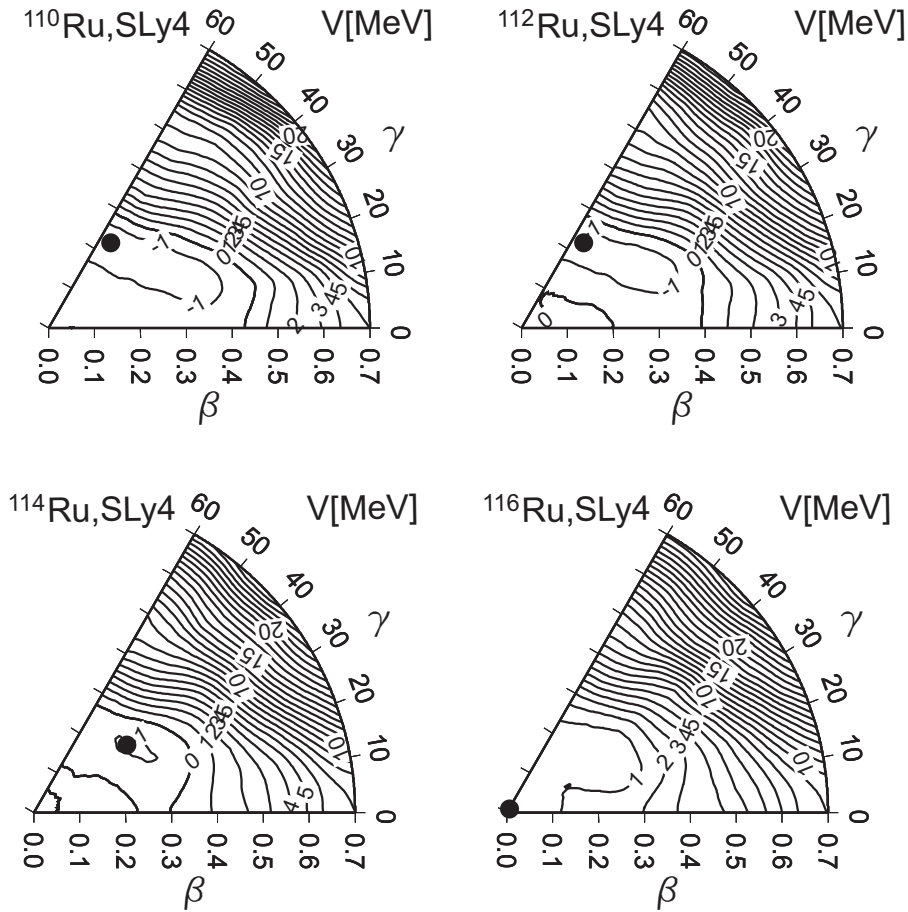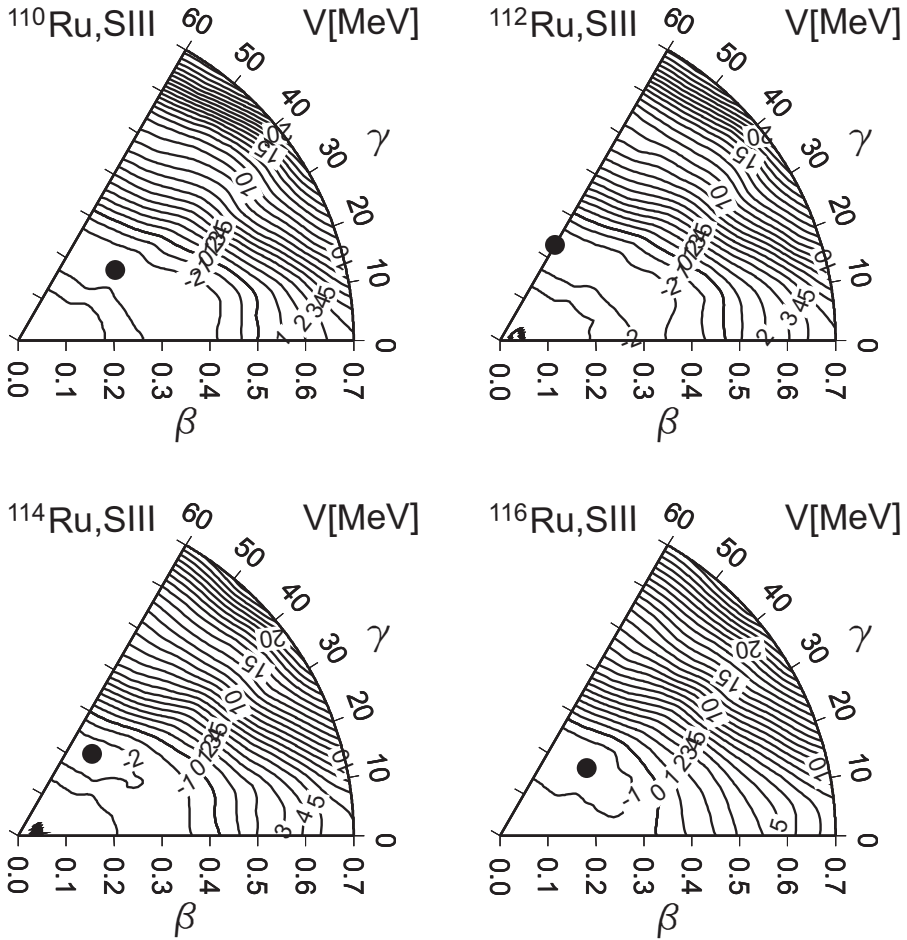
Figure 4.12: Potential energy surface plots for even ruthenium isotopes calculated with
the microscopic Bohr-Hamiltonian approach with the SIII type of Skyrme
interaction.

to the values for lighter ruthenium isotopes and the depths of the minima become shallower as N increases. The decreasing trend in experimental β values as N increases can also be observed.

Comparing Figs. 4.9 and 4.10, a change of the value and the sign of deformation can be observed since the palladium isotopes have weak prolate minima instead of γ-soft oblate shapes seen in the ruthenium isotopes. A shape evolution towards a spherical shape can be seen in silver–cadmium isotopes when heading towards the magic tin nuclei, see for example Ref. [115].

The Skyrme SLy4 interaction also predicts a spherical ground state for the ^{116}Ru isotope. In addition, the HFB approximation predicts spherical ground states for $^{118-124}$Ru isotopes, which can be due to the approach of the magic $N = 82$ closed shell [116]. These predictions are to be confirmed by future spectroscopic measurements. For example, the energy of the first 2^+ state and the energy ratio $E(4_1^+)/E(2_1^+)$ will be among the key observables in future studies.

Signature splitting function S(I) for ^{114}Ru

The shape of the triaxial potential can be studied with the signature splitting function $S(I)$ (Eq. (2.3)) of the γ band. In Fig. 4.13 the values of the $S(I)$ function derived from experimental level energies from this work and Ref. [117] have been compared to different theoretical predictions [33].

One can notice how the effective Skyrme interaction with the Sly4 parameterization corresponds very well with experimental values. The calculations with the SIII parameterization of the Skyrme interaction give a similar staggering corresponding to a very γ-soft shape whereas the staggering calculated from the rigid triaxial rotor model has the opposite trend. At low spins, no strong staggering can be seen in experimental values. At higher spins a somewhat stronger staggering towards a rigid triaxial shape can be observed. More rigid shapes at higher spins have been predicted theoretically in Refs. [21,118] although both predictions suggest more oblate shapes. A similar staggering pattern with ^{112}Ru [19] can be observed suggesting s similar shape for both isotopes.

The conclusion that can be drawn from Fig. 4.13 is that although the RTR model explains the B(E2) ratios reasonably well, it cannot explain the behavior of the $S(I)$ function. Based on the behavior of that function derived from the experimental level energies, the shape of the potential of ^{114}Ru is neither completely flat in the γ direction nor with a very well-localized deep minimum corresponding to the rigid
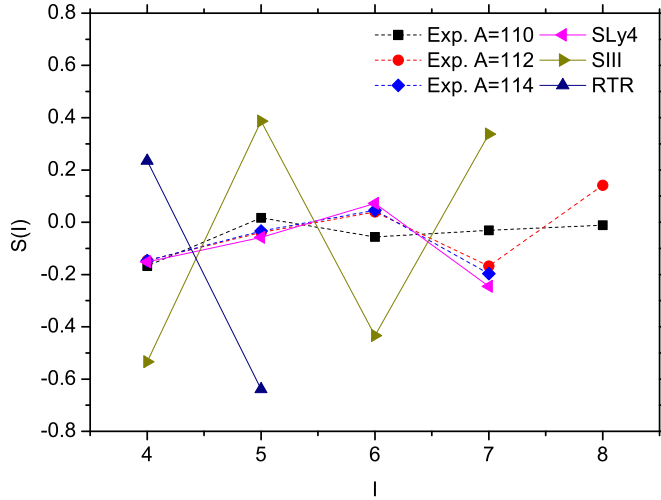
Figure 4.13: The signature splitting function of the gamma band. See text for more details.

triaxial shape. Instead, it has to be something in between these two extreme cases, which is also predicted by the HFB approximation and by the microscopic Bohr Hamiltonian approaches. In addition, the rigidity is increasing with increasing spin and the staggering of the ^{112}Ru and ^{114}Ru are very similar indicating similar triaxial nuclear shapes. This suggests that ^{114}Ru is still triaxial instead of a pure oblate shape, which is supported also by a recent experimental study [117].

4.3 ^{115}Ru beta decay

The ^{115}Ru beta decay was studied in two experiments within this work. The results of the first experiment, [Experiment 2], including an extended decay scheme and discussion about the structure of ^{115}Rh have been published in [Publication 5]. The results of another experiment, [Experiment 4], including the half-life of ^{115}Ru and discussion about the isomeric state in ^{115}Ru have been published in [Publication 3]. In this section some uncertain transitions will be reported and the ground state spin of ^{115}Ru will be discussed in more detail by comparing the experimental results to the predictions of the Triaxial Quasi-Particle Rotor model.

Table 4.6: Transitions possibly connected to the decay of ^{115}Ru but not placed in the decay scheme in [Publication 5]. The intensity of the 292.5-keV transition in ^{115}Rh has been normalized to 100 [Publication 5]. Weak transitions are in brackets.

E_γ (keV)	Intensity	Coincident lines
34.8(3)	0.9(3)	196.5 (No X-rays in coincidence)
47.4(2)	0.4(1)	(80.1), 207.0, (292.5), (638.3) ICC(K)=2.7(14)
668.0(7)	0.9(3)	207.0
776.5(7)	1.5(4)	207.0
1287.0(5)	1.1(4)	(80.1), 292.5, (372.5)
1800(1)	1.2(4)	292.5
1837(1)	1.5(4)	80.1, (292.5), 372.5
1895(1)	1.7(4)	292.5
1949.6(9)	1.5(3)	292.5
1964.6(6)	1.6(4)	292.5
2003.8(12)	1.5(4)	292.5
2149.4(7)	2.0(4)	80.1, 292.5
2175(1)	1.3(4)	292.5

4.3.1 Unplaced transitions related to the ^{115}Ru beta decay

The data collected in [Experiment 2] revealed transitions in coincidence with some transitions related to the decay of ^{115}Ru. However, these transition could not be placed in the decay scheme shown in [Publication 5], since some of the coincidence relations were unclear or missing. The transitions are reported in Table 4.6 and are to be confirmed by future measurements. The decay scheme of ^{115}Ru is presented in Fig. 4.14.

4.3.2 Spins of the ground state and isomeric state of ^{115}Ru

In [Publication 5] a ground state spin of $(3/2^+)$ for ^{115}Ru has been preferred to the $(1/2^+)$ assignment proposed in earlier publications [Publication 3] and [119]. The new spin assignment is based on the more accurately defined beta branchings and log ft values. A low ground state spin hints to oblate deformation, since the most
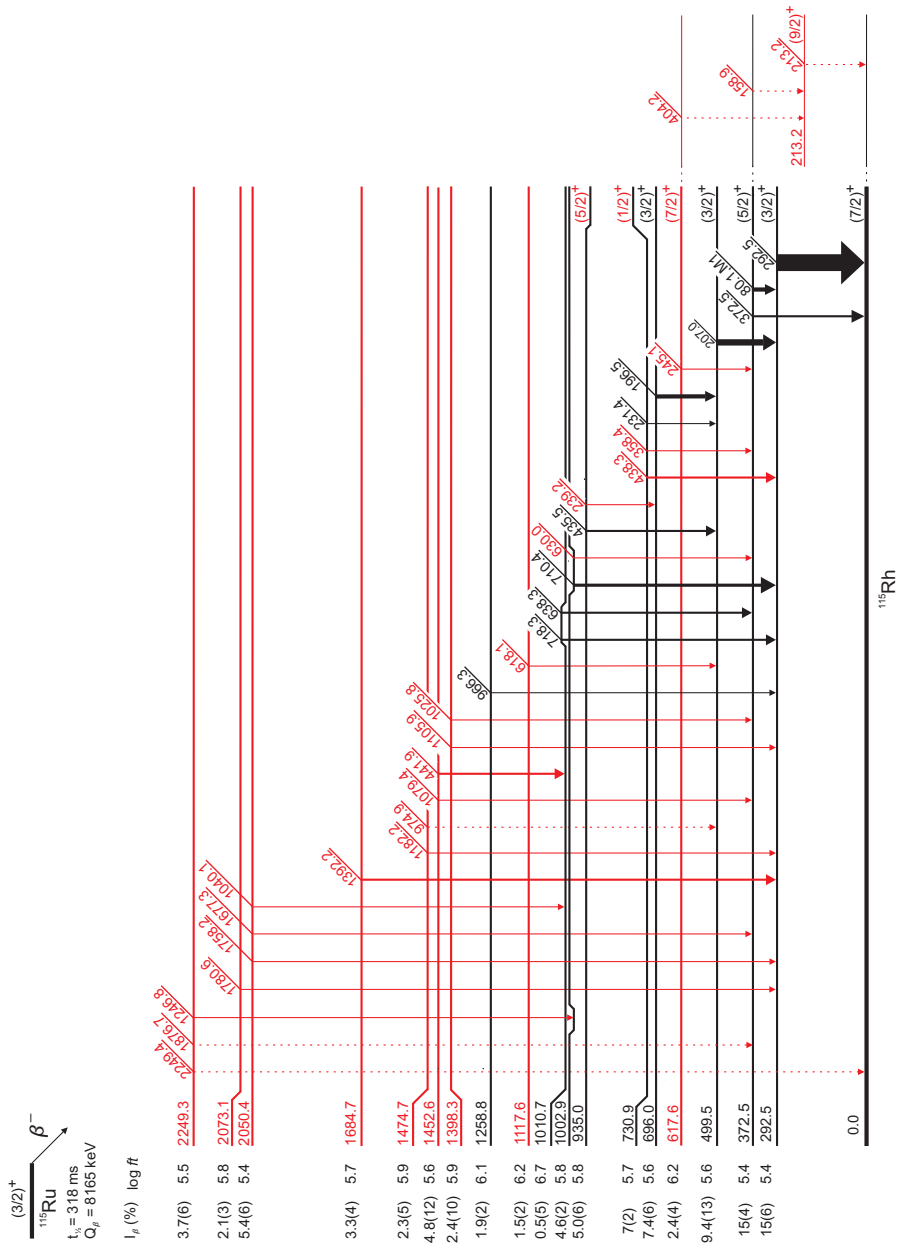
Figure 4.14: A beta-decay scheme of ^{115}Ru [Publication 5].
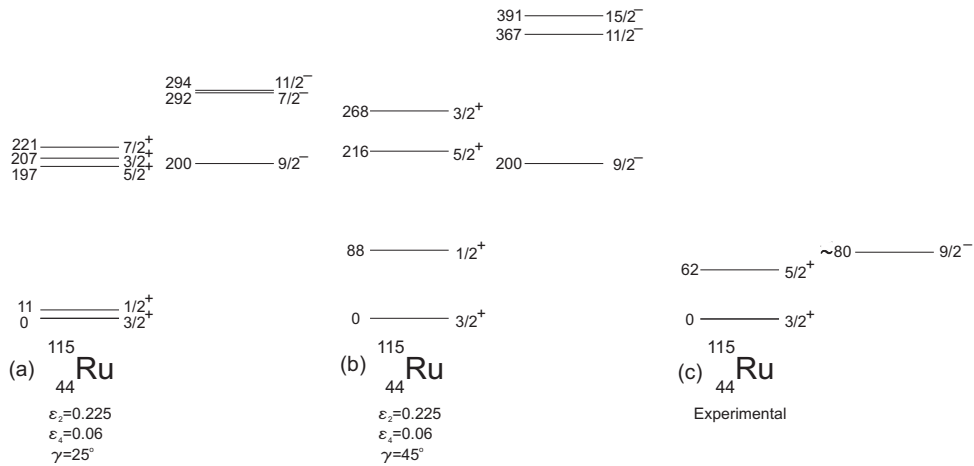
Figure 4.15: The lowest states in ^{115}Ru calculated with the Triaxial Quasi-Particle Rotor model [121] with two different sets of parameters. For the positive-parity states, $I = K$ except for the first $3/2^+$ state, which has $K = 1/2$. See text for more details.

probable orbitals, 1/2[411] and 3/2[402] for $1/2^+$ and $3/2^+$, respectively, are found on the oblate side of the Nilsson diagram at moderate deformation, see Fig. 4.6. The spins of the lowest levels in ^{115}Ru can be compared to the results of the Triaxial Quasi-Particle Rotor model calculations [120], see Fig. 4.15. The calculations have been performed by Dr. Gary Simpson from LPSC, Grenoble.

In the Triaxial Quasi-Particle Rotor model, the deformation parameters ϵ_2, ϵ_4, and γ, among some other parameters, have to be fixed beforehand [120]. In the calculations presented in Fig. 4.15, the ϵ parameters are taken from Ref. [122]. A parameter χ defines the strength of the Coriolis force [32]. For the parameter set (a) no Coriolis attenuation for positive-parity states and $\chi = 0.7$ for negative-parity states has been used. For the parameter set (b) $\chi = 0.7$ has been used. Both parametrizations reproduce the ground state spin of $3/2^+$, with the quantum number $K = 1/2$.

The model does not give reliable absolute energies for the positive and negative-parity bands and they need to be normalized to the experimental level energies. Since there is no experimental information about the negative-parity states in ^{115}Ru, the lowest negative-parity level has been normalized to 200 keV, which approximately corresponds to the energy of the $9/2^-$ isomeric state in ^{117}Pd.

The only experimentally observed gamma transition in ^{115}Ru is a 61.7-keV transition

with a half-life of 67 ms [Publication 3] and with an internal conversion coefficient $ICC = 2.7(6)$, which corresponds to a mixed M1 and E2 character of the transition. No gamma lines in coincidence with this transition were observed. Based on the half-life of the transition and an analogous structure in ^{113}Ru, a $(1/2^+)$ ground state, a $(3/2^+)$ intermediate state de-exciting via a 61.7-keV transition, and an isomeric $(7/2^-)$ state de-exciting via a non-observed converted M2 transition with an energy of about 20 keV, has been suggested in [Publication 3]. However, since there is more experimental evidence for the $3/2^+$ ground state, a sequence of the $3/2^+$ ground state in ^{115}Ru, the $5/2^+$ intermediate state, and the $9/2^-$ isomeric state seems to be more probable. The ground state spin of $3/2^+$ and the isomeric state spin of $9/2^-$ are supported by the Triaxial Rotor Model calculations. However, the spin of the intermediate state $(5/2^+)$ does not agree with the calculations. On the other hand, more experimental information is needed to optimize all the parameters of the model and the calculations have to be considered as tentative. To conclude, more experimental and theoretical work are needed to understand the structure of this very neutron-rich isotope.

4.4 ^{115}Rh beta decay

States in ^{115}Pd were fed in the beta decay of ^{115}Rh ($t_{1/2} = 0.99$ s [123]), a daughter of ^{115}Ru ($t_{1/2} = 318$ ms [Publication 3]). Since in [Experiment 2] the implantation tape was moved only once in 300 s, the total beta feeding to the states in ^{115}Rh was almost equal to the total beta feeding to the states in ^{115}Pd, and although the monoisotopic samples of ^{115}Ru isotopes were implanted into the tape, a reasonable amount of statistics concerning the second beta decay was collected.

A partial decay scheme, based on the data from [Experiment 2], was published already in [Publication 2], which concentrated on the shape transition in this region. In this chapter the extended beta-decay scheme of ^{115}Rh is presented and the new spin and parity assignments for the states in ^{115}Pd are proposed.

4.4.1 Overview of odd palladium isotope levels

Neutron-rich palladium isotopes are located in the region of a nuclear shape co-existence and a possible prolate-oblate shape transition. The shape coexistence was proposed some time ago [22,23], since the negative-parity high-spin isomer de-excites to the low-spin ground state via hindered transitions, which suggests the existence

of two different shapes. Also theoretical predictions including two potential minima exist, see for example Refs. [23, 115].

The exact location of the shape transition is uncertain, and in palladium isotopes it has been predicted to take place at ^{111}Pd [124]. However, this reference predicts the shape transition to happen already at $A=108$ in the ruthenium isotopic chain, instead of $A=111$ suggested in Refs. [26, 118, 125]. In Refs. [126, 127] the prolate shapes for the ground states of $^{108-112}$Pd have been suggested and in Ref. [128] no evidence for a prolate to oblate shape transition in the ^{113,115}Pd isotopes has been found, proposing that these isotopes have γ-soft prolate shapes. Also, Ref. [129] suggests prolate deformations for $^{113-117}$Pd isotopes. A prolate deformation is also supported by the theoretical results calculated with the HFB approximation with the D1S-type Gogny interaction, as shown in Fig. 4.10, where the PES plots for $^{110-116}$Pd isotopes exhibit weak prolate shapes. It is noted in Ref. [116] that the same theoretical approach predicts prolate ground states even for more neutron-rich $^{118-120}$Pd isotopes. After this brief literature survey, the prolate-oblate shape transition suggested to take place in this region seems not to extend to neutron-rich palladium isotopes.

The ground state spins of $5/2^+$, $1/2^+$, and $3/2^+$ for ^{113}Pd, ^{115}Pd, and ^{117}Pd, respectively, have been proposed in Ref. [130]. This sequence can be seen in ruthenium isotopes at the same neutron numbers. In the ruthenium isotopic chain, this sequence could be related to the shape transition, as discussed in [Publication 2] and [Publication 5]. The most probable configurations for these spin assignments are the 5/2[402], 1/2[411], and 3/2[402] Nilsson orbitals, from which the 5/2[402] configuration is located on the prolate side and the 3/2[402] on the oblate side of the Nilsson diagram. Thus, a shape transition taking place between $A = 113$ and 117 can be suggested based on the Nilsson model, which is contrary to the above-mentioned experimental observations and theoretical predictions. On the other hand, since the $1/2^+$ and $3/2^+$ ground state configurations have been suggested also for vibrational cadmium and spherical tin isotopes at neutron numbers $N = 69$ and 71, respectively, the ground state spin transition could also be an indication of a shape transition towards spherical shapes. If considering only the spherical shell model states, the $3s_{1/2}$ and $3d_{3/2}$ spherical orbits are close to the Fermi level at $N = 70$. However, it is clear that more theoretical and experimental work is needed for a final conclusion.

Figure 4.16: The beta-decay scheme of ^{115}Rh. The gammas and levels in red are new, those in green have been presented already in [Publication 2], and those in blue have been seen in the earlier beta-decay work of Ref. [131] but have not been published.

Table 4.7: Excited levels in ^{115}Pd fed by the beta decay of ^{115}Rh. The beta feeding to
the 50-s isomeric state at 89.3 keV cannot be derived from our data. The level
energies may differ slightly from the ones in [Publication 2] due to different
calibrations used.

E_{level} (keV)	β-feeding (%)	$\log ft$	I^π
89.3(3)	-	-	$(7/2^-)$
127.8(3)	5.0(6)	6.0(1)	$(9/2^-)$
127.9(2)	~ 0	-	$(3/2^+)$
235.2(2)	~ 0	-	$(1/2\text{-}3/2^+)$
253.8(2)	28(5)	5.1(1)	$(5/2^+)$
269.9(2)	~ 0	-	$(1/2\text{-}3/2^+)$
295.8(2)	6(1)	5.8(2)	$(5/2^+)$
354.8(2)	5.2(11)	5.8(2)	$(7/2^+)$
406.6(2)	2.3(10)	6.1(2)	$(3/2^+)$
433.6(2)	23(5)	5.1(1)	$(5/2\text{-}7/2^+)$
468.2(2)	5.4(4)	5.8(1)	$(7/2^+)$
576.5(2)	5.7(10)	5.7(1)	$(7/2^+)$
655.0(2)	2(2)	6.0(3)	
703.2(2)	1.2(3)	6.3(2)	
917.7(2)	5.3(11)	6.5(3)	
919.3(2)	3.3(6)	5.8(1)	$(5/2\text{-}7/2^+)$
1339.6(2)	12.3(10)	5.1(1)	$(5/2\text{-}7/2^+)$
1605.0(4)	1.9(4)	5.8(1)	$(5/2\text{-}9/2^+)$

Table 4.8: Gamma rays following the beta decay of ^{115}Rh. The intensity of the 292.5-keV transition in ^{115}Rh has been normalized to 100 [Publication 5]. The intensity values have been corrected for internal conversion. The notation ^{t} means that the multipolarity is the most probable based mostly on the spin differences between the levels and the internal conversion coefficient has been taken from Ref. [59]. The notation ^{x} means that the 125.8-keV and 127.9-keV transitions could not be resolved. The gamma-ray energies may differ slightly from the ones in [Publication 2] due to different calibrations used.

E_γ (keV)	Intensity	Multipolarity	Coincident lines
38.6(2)	5.5(5)	M1^t	-
61.1(2)	2.7(10)	M1^t	235.2, (279.7), (407), ICC(K)$\approx$ 1.5(7)
101.0(2)	7.8(10)	M1(/E2) [131]	K$_\alpha$(Pd), 125.8, 127.9, 164.5, 221.8, 253.8, 984.7, 1086.0
125.8(2)	50(4)	M1(/E2) [131]	K$_\alpha$(Pd), 101.0, 127.9, 153.3, 179.8, 221.8, 322.7, 400.6, 665.1, 984.7, 1086.0, 1350.9
127.9(2)	68(4)	M1/E2 [131]	K$_\alpha$(Pd), 101.0, 125.8, (153.3), 179.8, 227.0, 278.7, 305.6, 322.7, 400.6, (665.1), 789.8, 984.7, 1086.0, 1171.7, 1212.3, 1350.9
136.5(3)	0.8(8)	M1^t	269.9
137.7(2)	4.4(3)	M1^t	K$_\alpha$(Pd), 164.5, (235.2), 295.8
153.3(2)	1.2(3)	M1^t	(125.8+127.9)^x
163.5(9)	3(3)	M1/E2^t	269.9
164.5(2)	15(4)	E1^t	K$_\alpha$(Pd), 101.0, 179.8, 322.7, (400.6), 1086.0
179.8(2)	16(3)	M1 [131]	K$_\alpha$(Pd), 125.8, 127.9, 164.5, 253.8, 1171.7
198.4(2)	2.9(4)	E2^t	K$_\alpha$(Pd), 235.2
221.8(3)	1.1(4)	M1^t	101.0, 227.0, 265.3
227.0(5)	1.1(2)	E2^t	127.9, 984.7
235.2(2)	8.6(5)	M1^t	61.1, 198.4, 684.5, 1104.5
253.8(2)	7.3(10)	E2^t	101.0, 179.8, 400.6, 1086.0
265.3(2)	2.7(5)	E1^t	-
269.9(2)	7.2(4)	E1^t	K$_\alpha$(Pd), 136.5, 163.5, 647.8, 1069.6
278.7(2)	1.0(5)	M1^t	127.9
279.7(7)	1.7(6)	M1,E2^t	295.8
295.8(2)	12.2(7)	E2^t	137.7, 279.7, 407.4, 1044.4
305.6(2)	3.2(6)	E2^t	K$_\alpha$(Pd), 127.9,
322.7(2)	1.4(2)	M1,E2^t	125.8, 127.9, 164.5, 253.8
340.3(2)	6.7(5)	-	127.9

Table 4.8: – Continued from previous page

E_γ (keV)	Intensity	Multipolarity	Coincident lines
400.6(2)	2.8(3)	-	125.8, 127.9, 253.8
407.4(2)	1.5(3)	-	295.8
448.9(2)	2.8(10)	-	K$_\alpha$(Pd), 127.9
647.8(3)	0.4(4)	-	(269.9)
665.1(3)	2.0(5)	-	K$_\alpha$(Pd), 125.8, 127.9
684.5(3)	2.1(6)	-	235.2
789.8(2)	0.6(2)	-	K$_\alpha$(Pd), 127.9
984.7(2)	4.0(6)	-	101.0, 127.9, (227.0)
1044.4(5)	1.1(3)	-	(295.8)
1069.6(5)	0.6(3)	-	269.9
1086.0(3)	4.8(7)	-	125.8, 127.9, 164.5, 253.8
1104.5(3)	2.8(5)	-	235.2
1171.7(6)	1.5(5)	-	125.8, 127.9, 164.5, 179.8, 198.4,
			(235.2), 253.8, (269.9), (295.8)
1212.3(9)	2.0(6)	-	127.9
1350.9(6)	0.8(2)	-	K$_\alpha$(Pd),125.8, 127.9

4.4.2 Spin and parity assignments of the excited levels in ^{115}Pd

The gamma transitions identified in this work which belong to the decay of ^{115}Rh
are presented in Table 4.8 and the excited levels in ^{115}Pd are shown in Table 4.7. In
this subsection the suggested spin assignments for different levels are discussed.

The ground state $(1/2^+)$. The spin and parity assignment for the ground state have
been derived from the spin and parity of the $(7/2^-)$ isomeric state. The isomeric
transition has a multipolarity of E3 and a half-life of 50 s [132], and therefore $1/2^+$
is the obvious assignment for the ground state. This level probably has a 1/2[411]
Nilsson configuration originating from the $3s_{1/2}$ spherical orbit, which has been
identified to exist close to the ground state in lighter palladium isotopes. Since the
beta-decaying ground state of ^{115}Rh has a spin of $(7/2^+)$, a negligible ground-state
beta feeding is assumed to this state.

The 89.3-keV level $(7/2^-)$. This level is an isomeric state with a half-life of 50 s [132]

and with a configuration of $7/2^-[523]$ from the $1h_{11/2}$ spherical orbit. The beta feeding to this level cannot be derived from our data. However, it cannot be large due to a parity change, corresponding to the first forbidden beta transition. These transitions have a log ft value of the order of 7, which in this case would correspond to a beta branching less than 0.5 %.

The 127.8-keV level $(9/2^-)$. This level de-excites by a 38.6-keV transition, which can be seen in the singles spectrum. The intensity of the 38.6-keV transition defines the log ft value of the beta decay to this level (log $ft = 6.0$), which is a rather small value for the first forbidden $7/2^+ \rightarrow 9/2^-$ transition, suggesting that the intensity of the 38.6-keV transition may be overestimated. Since the 38.6-keV transition can be seen in beta decay, it suggests the spin assignment of $(9/2^-)$ for this level and the assignment of $(7/2^-)$ for the 89.3-keV level. Furthermore it fixes the ground state spin to $(1/2^+)$, as proposed also in Refs. [98, 130]. See [Publication 2] for a more detailed discussion.

The 127.9-keV level $(3/2^+)$. The spin-parity of this level has been defined in [130]. It can have a 3/2[402] Nilsson configuration, see Fig. 4.17 and related discussion.

The 235.2-keV level $(1/2^+, 3/2^+)$. This level has not been observed in earlier beta-decay works [131]. A 235-keV transition de-exciting from this level has been seen in Ref. [131] and a 198-keV transition populating this level has been seen but not located in the decay scheme in Refs. [123, 131]. This level is not fed by the beta decay of the $(7/2^+)$ ground state of ^{115}Rh, which indicates that the spin of this level is probably smaller than $5/2^+$. It has connections to the $(1/2^+)$ ground state and to the excited states at 295.8 keV $(5/2^+)$ and 433.6 keV and 1339.5 keV $(5/2^+, 7/2^+)$. Connections to the 253.8-keV and 269.9-keV levels were not observed in this work. These possible transitions would be highly converted and would need a high-resolution conversion electron measurement to be observed. Spin assignments of $(1/2^+, 3/2^+)$ have been suggested, from which the $(1/2^+)$ spin assignment would fix the spins of the 433.6-keV and 1339.5-keV levels to $(5/2^+)$ and the $(3/2^+)$ assignment to $(7/2^+)$, respectively.

The 253.8-keV level $(5/2^+)$. The $(5/2^+)$ spin assignment is known from prompt fission studies [98, 130]. This level is so strongly fed by beta decay (log $ft = 5.1$) that it may not be a member of a $K = 1/2$ ground state band. Belonging to that band would indicate a K-forbidden beta transition, which would have much larger log ft values than allowed transitions. However, in triaxial nuclei, the K-parameter is not a good quantum number, and the K-forbidden transitions are not as retarded as in the case of heavy nuclei, see for example [48]. Since the log ft value is 5.1 for the

transition populating this state, no retardation is observed.

Strongly fed first excited $5/2^+$ states have also been observed in lighter palladium isotopes. In Refs. [22,131] the strong feeding has been explained by these states having origin from the first 2^+ state in the even palladium core coupled to an unpaired neutron in the $d_{5/2}$ or $g_{7/2}$ orbital. This needs to be confirmed, since both spherical states are below the Fermi level in ^{115}Pd.

The 269.9-keV level $(3/2^+)$. This level has not been observed in earlier studies. The 270-keV gamma transition has been observed in Refs. [123,131] but not placed in the decay scheme. In addition to the connection to the $(1/2^+)$ ground state, it is connected to the $(3/2^+)$ state at 406.6 keV and $(5/2^+, 7/2^+)$ states at 433.6 keV and 1339.5 keV. It is not fed by beta decay and therefore $(5/2^+)$ spin assignment is not probable and $(3/2^+)$ was chosen.

The 136.5-keV transition is in coincidence with the 269.9-keV transition and it is placed between the 406.6-keV and 269.9-keV levels. Another possibility is that there is a non-observed transition between the levels at 295.8 keV and 269.9 keV and the 137.7 keV transition is seen in coincidence with the 269.9 keV transition. A final conclusion about this transition needs a high-resolution conversion electron measurement, which helps to see the converted low-energy transitions.

The 295.8-keV level $(3/2^+, 5/2^+)$. This level has connections to the $(1/2^+)$ ground state and to several excited states. It was found in Ref. [131] with a beta feeding of 13.2 % and log ft value of 5.6 with only one gamma transition populating this level. In this work the somewhat different values for beta feeding (6 %) and for log ft (5.8) have been found, which are due to new gamma transitions populating this level. The conversion electron measurement from Ref. [131] suggests $L = 1$ (M1 or E1), which would fix the spin of the level to 3/2. However, if the log ft value is <6.0, the beta transition to this level is considered as an allowed transition and the spin of 3/2 is not possible. One has to keep in mind that in this nuclide there are several states close in energy. Therefore, there can exist also highly converted low-energy transitions not seen in gamma spectra, which may change the intensity ratios between the levels. A high-resolution conversion electron measurement is needed for the definition of the precise intensity ratios.

The 354.8-keV level $(7/2^+)$. The spin of this level was already known from earlier works [123,131]. This work supports also the $(7/2^+)$ spin assignment.

The 406.6-keV level $(3/2^+)$. This level is only weakly fed by beta decay. Is has a strong connection to the $(3/2^+)$ state at 127.9 keV and tentative weaker connections

to the levels with spins of $(3/2^+)$–$(5/2^+)$. There is also a 407-keV transition populating the 295.8-keV level. Part of the intensity of this transition may belong also to the transition from the 406.6-keV level to the ground state. The $(3/2^+)$ assignment is adopted, which fits well to the systematics of the lighter palladium isotopes.

The 433.6-keV level $(5/2 - 7/2)^+$. This level is fed by beta decay with a log ft of 5.1 (5.2 in Ref. [123]) indicating $5/2^+ \leq I^\pi \leq 9/2^+$. It has connections to the $(3/2^+)$–$(5/2^+)$ levels but no connection to the $(1/2^+)$ ground state. These arguments limit the possible spin assignments to $(5/2^+)$ or $(7/2^+)$. The $(5/2^+)$ assignment enables the $(1/2^+)$ assignment for the 235.0-keV state and suggests also the $(5/2^+)$ assignment for the 295.8-keV and 1339.5-keV levels. Non-observation of the ground state transition hints to the $(7/2^+)$ assignment for this level. On the other hand the $(7/2^+)$ assignment shifts the above mentioned spin assignments one unit upwards. A possible Nilsson configuration for this level could be 7/2[404], see discussion related to the 1339.5-keV level.

The 468.2-keV level $(7/2^+)$. This level is fed by beta decay with a log ft value of 5.8, which limits the possible spins to this level to $5/2 - 9/2^+$. Since it has a connection to the $(3/2^+)$ level at 127.9 keV, it has probably a spin lower than or equal to 7/2. In Ref. [129] a rotational band has been seen based on this level. Assuming an E2 nature for the intraband transitions, the next level of this band locate at 956.5 keV de-excites by a 488.4 keV transition. This transition is not seen in our study, which suggests that the spin of the 956.5-keV level cannot be $5/2^+ - 9/2^+$. Assuming a higher spin than 9/2 for the 956.5-keV level, the spin of the 468.2 keV level has to be 7/2 or higher. The only possible spin assignment is $(7/2^+)$. However, no connection to other levels have been found, which makes this assignment a bit uncertain.

The 576.5-keV level $(7/2^+)$. In [Publication 2] a spin of $(9/2)^+$ has been assigned for the level at 575.5 keV. No connection from that level to the 127.9-keV and 295.8-keV levels were reported. Since the 449.4-keV transition to the 127.9-keV level $(3/2^+)$ has been observed in this work, the $(9/2^+)$ assignment is not very probable due to a large spin difference. The 449.4-keV transition has the highest intensity among the transitions depopulating this level, which means that it cannot be due to a coincidence summing.

The 917.7-keV level Two levels have been found to locate around 918 keV. The lower level has connections to the $(3/2^+)$ state at 127.9 keV and to the $(5/2^+)$ state at 295.8 keV, suggesting a low spin for this level. A log ft value of 6.5 hints to a first forbidden beta transition. However, no good candidate for the spin assignment for this level has been found.

The 919.3-keV level $(5/2 - 7/2)^+$. This level has connections to levels with spins of $(3/2^+ - 5/2^+)$. Also an allowed beta transition to this level with a log ft value of 5.8 was observed. These arguments suggest the spins of $(5/2^+ - 7/2^+)$ for this level.

The 1339.5-keV level $(5/2 - 7/2)^+$. This level was seen in Ref. [131], de-exciting via three gamma transitions (1212-keV, 1087-keV, and 986-keV). In this work three additional gamma lines were observed depopulating this level. It is fed by beta decay with a log ft of 5.1. This kind of level with a strong beta feeding has not been observed in decays of lighter rhodium isotopes. One possible configuration for this level is a 7/2[404] originating from a $1g_{7/2}$ spherical orbit on the prolate side of the Nilsson diagram. This configuration would be fed by beta decay of the 7/2[413] configuration with a relatively low log ft value ($\Delta\Omega = 0, |\Delta N| = 0, |\Delta n_z| = 1, |\Delta\Lambda| = 1$). On the other hand, the same configuration should exist also in lighter palladium isotopes. One reason for the non-observation could be that in previous beta decay studies, smaller Ge detectors have been used, which have small efficiency for the high-energy gamma rays. Another possibility is that the 7/2[404] configuration is for the 433.6-keV level, which also has a low log ft value (5.1). Since this level also has a connection to the 235.2-keV level with a possible spin of $(1/2^+)$, the $(5/2^+)$ is also possible and an unambiguous spin definition cannot be made.

The transitions not placed in the level scheme in Ref. [131]

In Ref. [131] 12 gamma transitions have been found but not placed in the decay scheme of ^{115}Rh. Since we have cleaner spectra resulting from the utilization of the Penning trap as a high-resolution mass filter, most of these transitions could be located in the decay scheme. In this work, the 38.5-keV, 138-keV, 198.4-keV, 235.3-keV, 270.1-keV, 281-keV, and 400.9-keV transitions could be placed in the decay scheme. In addition, the 172-keV, 205-keV, 462-keV, and 883.4-keV transitions were not seen in our study and the 247-keV, 423.6-keV, and 498-keV transitions could be assigned to the decay of ^{115}Pd.

4.4.3 Level systematics of odd neutron-rich palladium isotopes

The level systematics of odd neutron-rich palladium isotopes are shown in Fig. 4.17. The density of the levels at low energies is rather high and the spin assignments of some levels are uncertain. Therefore the spin assignments of ^{115}Pd based on the systematics are also to be confirmed.
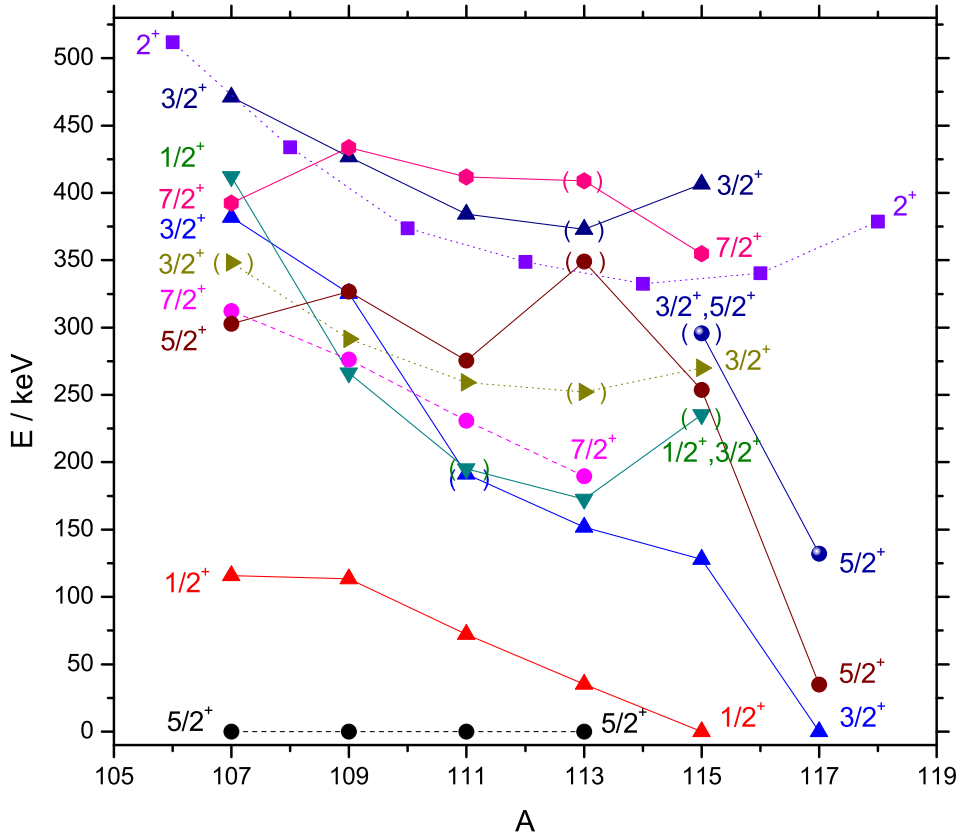
Figure 4.17: Positive-parity level systematics of odd-mass neutron-rich palladium isotopes. Also the lowest 2^+ levels in even palladium isotopes are shown. The $(5/2^+)$ and $(7/2^+)$ states possibly built on the 5/2[402] excitation are connected with dashed lines. The 2^+ states in even palladium isotopes and the $(3/2^+)$ states in odd palladium isotopes having a similar behavior are connected with dotted lines. One can notice how there are several states located below $E = 500$ keV and therefore the spin assignments based on the level systematics are somewhat uncertain.

The ground states of $^{107-113}$Pd isotopes ($61 \leq N \leq 67$) probably have the 5/2[402] Nilsson configuration originating from the $g_{7/2}$ spherical orbit. Also the lowest ($7/2^+$) states in these isotopes belongs to the band structure based on the same configuration. At $N = 69$ the Fermi level reaches the 1/2[411] orbital originating from the $3s_{1/2}$ spherical orbit, and therefore the ($5/2^+$) and ($7/2^+$) states probably based on the 5/2[402] configuration are not observed in ^{115}Pd.

The 1/2[411] orbital could become the ground state configuration for ^{115}Pd, see [Publication 2]. This Nilsson orbital has been observed in lighter palladium isotopes, since the 72-keV level in ^{111}Pd has been assigned to the $s_{1/2}$ single-particle state (1/2[411] Nilsson state), in an analogy with the 116-keV and 113-keV levels in ^{107}Pd and ^{109}Pd, respectively.

The next Nilsson state is the 3/2[402] orbital originating from the spherical $2d_{3/2}$ orbit, which could be the configuration of the 127.9-keV level in ^{115}Pd and can become the ground state configuration for ^{117}Pd at $N = 71$. The same configuration has been suggested for the ground state of ^{115}Ru in [Publication 5].

The behavior of the ($3/2^+$) levels (at 269.9 keV and 406.6 keV in A=115) is similar and they correlate with the energies of the first 2^+ states in even palladium isotopes. One explanation for that could be that the ($3/2^+$) state originates from the first 2^+ state of the even palladium core coupled to the odd neutron in the $g_{7/2}$ orbital. However, more theoretical and experimental work is required for the unambiguous identification of the structure of these states.

A spin ($1/2^+$)-state has been observed in ^{109,113}Pd isotopes at low energies (at 266.3 keV in ^{109}Pd and at 172.6 keV in ^{113}Pd). A candidate for the ($1/2^+$) spin assignment is also seen in ^{111}Pd at around 190 keV. It is an interesting question whether the same state exist also in ^{115}Pd. A 235.2-keV level could be a candidate for that state, being the lowest level with an unknown spin. In that case the trend of the ($1/2^+$) level seems to go up in energy.

5 Summary and outlook

In this work, neutron-rich fission products were studied by means of Penning-trap-assisted spectroscopy. These studies were linked by the utilization of a Penning trap as a mass filter to purify the mass-separated IGISOL beam to a monoisotopic level and subsequent detection of radiation of different types from the purified ion samples with different detectors. The β-γ coincidence measurements were used to study the beta decays of very neutron-rich isotopes ^{115}Ru, ^{115}Rh, and ^{114}Tc. In addition to the β-γ studies, new techniques including conversion electron spectroscopy of the trapped radioactive ions and neutron spectroscopy with the BELEN-20 detector with monoisotopic radioactive sources were introduced.

The ^{115}Ru isotope is the most neutron-rich ruthenium isotope presently available for spectroscopic studies at IGISOL. Its decay was studied in two experiments, from which the first resulted in an extended decay scheme and the discovery of a new gamma-decaying isomeric state in ^{115}Ru. The second experiment resulted in new half-life values for both states. Based on the observed beta feedings and log ft values, a spin value of $(3/2^+)$ was preferred to the previously reported $(1/2^+)$ for the ground state of ^{115}Ru. This important result also helped to suggest a spin of $(9/2^+)$ for the isomeric state. The ground state spin value can correspond to the 3/2[402] Nilsson state on the oblate side of the Nilsson scheme, which is consistent with the predicted prolate-oblate shape transition. These values are still to be confirmed, especially for the isomeric state.

The ^{114}Tc isotope is the most exotic isotope studied by means of trap-assisted spectroscopy, having a yield of only 3 ions/s measured with the MCP detector located after the trap. However, due to a pure radioactive sample, the first beta-decay scheme for this nuclide could be built, which revealed the existence of two beta-decaying states. The observed isomeric state is the first beta-decaying isomer found in the technetium isotopic chain. The spin of one state was defined to be 1^+ whereas the spin the second state has to be 4 or higher. The Gallagher-Moszkowski rule suggest the 1^+ state to be the ground state. The half-life values for both states were measured to be close to each other and the Q_β value associated with a mixture of both states has been measured with JYFLTRAP to high precision.

As a byproduct, the decay of ^{115}Rh, the daughter of ^{115}Ru was also studied. In this case, the beta-decay scheme was substantially extended and the spins of the ground state and the isomeric state were defined, which confirm the old values suggested based on the prompt gamma spectroscopy studies.

The feasibility of JYFLTRAP for in-trap conversion electron spectroscopy was also tested in this work. Several conversion electron spectra from trapped radioactive ions, including spectra from ^{117m}Pd, ^{118m,120m}Ag, and ^{118m}In, were measured. The measured spectra are probably among the best-quality conversion electron spectra ever measured with semiconductor detectors, which prove the feasibility of this technique. In addition, simulations related to the detector setup were performed suggesting that the detection efficiency of the setup was limited due to the detector size in [Experiment 1].

In addition, a new Long-Counter-type neutron detector BELEN-20 was tested in connection to the JYFLTRAP setup. The testing was performed in two different experiments and the data analysis is still in progress. However, these tests proved the feasibility of the technique and some preliminary results have already been published [96, 97]. The test experiments revealed some problems in positioning of the beam spot inside the neutron detector, which could be solved with better ion optics after the trap.

With the methods used in this work, one can build a relatively complete picture about the beta decay of the nuclide-of-interest. The β-γ coincidence studies provide the main bulk of data for constructing the beta-decay schemes and the measured Q_β values define the beta-decay energy windows. The detected neutrons define the beta-delayed neutron probability, which reduces the amount of missing beta intensity and helps to define the ground-state beta feeding more reliably. However, the Pandemonium effect, which means that the beta decay populates high-lying states de-exciting via unobserved low-intensity transitions, still limits the accuracy of the measured beta feedings. This problem can be partially solved by using larger Ge detectors or via the Total Absorption spectroscopy (TAS) method, which measures the total gamma intensity of the decay from which the beta feedings to the different states can be extracted. In this case the data analysis is rather difficult, but the isobaric background can be drastically reduced by utilizing monoisotopic sources, which makes the analysis easier. Experiments with the TAS detector connected with the JYFLTRAP setup have already been successfully performed [133]. Removing the isobaric background is an important issue also for the neutron measurements.

Some additional value for spectroscopic measurements can be gained by introducing

a conversion electron detector in the detector setup, since the definition of the internal conversion coefficient also defines the multipolarity of the transition and helps to select the correct spins and parities for the low-energy levels. The detector can be placed either inside the Penning trap or in the spectroscopy setup located after the trap. If the conversion electrons are detected with the detector in the post-trap spectroscopy setup, the coincidence measurements become easier but it deteriorates the quality of the electron spectra. In the in-trap case the quality of the spectra is better but the coincidence measurements are more complicated. The ce-ce and β-ce coincidence measurements require a special segmented electron detector and the γ-ce or β-γ-ce measurements are even more complicated due to a high magnetic field and limited space inside the bore of the trap magnet. If these techniques become feasible, the simultaneous in-trap gamma-ray and conversion electron measurements could provide the perfect tool for internal conversion coefficient measurements. The segmented conversion electron detector can be also used as a trap diagnostics tool to define the size and the location of the ion cloud inside the trap and enable the removal of the sum peaks in the conversion electron spectra.

One has also to keep in mind that even without any coincidence measurement, due to the quality of the spectra measured with the existing silicon detector, precise definitions of the K/L conversion electron ratio can be performed and the conversion coefficients can be calculated. In future measurements the possibility to move the detector conveniently in and out positions is important, since it allows the conversion electron measurements when needed and does not disturb the mass measurements. Another practical improvement, the use of a pulse-down drift tube would allow the lowering of the trap high voltage to the ground potential, which would help in data collection.

The trap-assisted spectroscopy results provide a complementary method to collinear laser spectroscopy measurements, which are very powerful in determining the deformation and the spins of the studied nuclei. The level structure of the isotopes-of-interest can be further studied by level lifetime measurements, which could help in defining the hindrance factors of the studied transitions. From these factors one could define which transitions are between the different shapes, which is added important information in the region of shape coexistence. In addition, a superior method to purify the beam to the isomeric level, a Ramsey cleaning method, is one attractive possibility for the in-trap and post-trap spectroscopy experiments.

Within the last few years trap-assisted spectroscopy has become a standard method to study the properties of very neutron-rich nuclei. When writing this thesis, the building of the new IGISOL beam lines located in the new experimental hall is in

progress. With the help of upgraded beam intensities provided by a new MCC30/15 cyclotron, the spectroscopic studies of the neutron-rich refractory elements can be extended even to more neutron-rich cases compared to the nuclei studied in this work.

Bibliography

[1] http://research.jyu.fi/igisol/JYFLTRAP_masses/.

[2] T. Eronen *et al.*, Phys. Lett. B **636**, 191 (2006).

[3] T. Eronen *et al.*, Phys. Rev. Lett. **97**, 232501 (2006).

[4] T. Eronen *et al.*, Phys. Rev. Lett. **100**, 132502 (2008).

[5] T. Eronen *et al.*, Phys. Rev. C **79**, 032802 (2009).

[6] T. Eronen *et al.*, Phys. Rev. Lett. **103**, 252501 (2009).

[7] U. Hager *et al.*, Phys. Rev. Lett. **96**, 042504 (2006).

[8] U. Hager *et al.*, Phys. Rev. C **75**, 064302 (2007).

[9] U. Hager *et al.*, Nucl. Phys. A **793**, 20 (2007).

[10] J. Hakala *et al.*, Phys. Rev. Lett. **101**, 052502 (2008).

[11] S. Rinta-Antila, Ph.D. thesis, University of Jyväskylä, 2006.

[12] S. Rinta-Antila *et al.*, Eur. Phys. J. A **31**, 1 (2007).

[13] J. Stachel *et al.*, Nuclear Physics A **383**, 429 (1982).

[14] J. Stachel *et al.*, Z. Phys. A **316**, 105 (1984).

[15] J. Äystö *et al.*, Nuclear Physics A **515**, 365 (1990).

[16] D. Troltenier *et al.*, Nuclear Physics A **601**, 56 (1996).

[17] K. Zajac *et al.*, Nuclear Physics A **653**, 71 (1999).

[18] J. C. Wang *et al.*, Phys. Rev. C **61**, 044308 (2000).

[19] I. Stefanescu *et al.*, Nuclear Physics A **789**, 125 (2007).

[20] Y. Luo *et al.*, Physics Letters B **670**, 307 (2009).

[21] F. R. Xu, P. M. Walker, and R. Wyss, Phys. Rev. C **65**, 021303 (2002).

[22] H. Penttilä *et al.*, Nuclear Physics A **561**, 416 (1993).

[23] J. Äystö *et al.*, Nuclear Physics A **480**, 104 (1988).

[24] E. M. Burbidge, G. R. Burbidge, W. A. Fowler, and F. Hoyle, Rev. Mod. Phys. **29**, 547 (1957).

[25] Y. Z. Qian, Progress in Particle and Nuclear Physics **50**, 153 (2003).

[26] C. Y. Wu *et al.*, Phys. Rev. C **73**, 034312 (2006).

[27] E. Caurier *et al.*, Rev. Mod. Phys. **77**, 427 (2005).

[28] S. G. Nilsson, Mat. Fys. Medd. Dan. Vid. Selsk. **26**, (1955).

[29] K. S. Krane, *Introductory Nuclear Physics* (Wiley, New York, 1987).

[30] R. Firestone and V. Shirley, *Table of Isotopes* (Wiley, New York, 1996).

[31] A. Bohr and B. Mottelson, *Nuclear Structure, vol 2, p. 33* (Benjamin, New York, 1975).

[32] R. Casten, *Nuclear Structure from a Simple Perspective* (Oxford University Press, Oxford, 1999).

[33] L. Próchniak, private communication, 2010.

[34] L. Wilets and M. Jean, Phys. Rev. **102**, 788 (1956).

[35] A. S. Davydov and G. F. Filippov, Nuclear Physics **8**, 237 (1958).

[36] N. V. Zamfir and R. F. Casten, Physics Letters B **260**, 265 (1991).

[37] L. Grodzins, Physics Letters **2**, 88 (1962).

[38] L. Esser, U. Neuneyer, R. F. Casten, and P. von Brentano, Phys. Rev. C **55**, 206 (1997).

[39] H. Morinaga and T. Yamazaki, *In-beam Gamma-Ray Spectroscopy* (North Holland, Amsterdam, 1976).

[40] F. Iachello and A. Arima, *The Interacting Boson Model* (Cambridge University Press, Cambridge, England, 1987).

[41] J. Stachel, P. Van Isacker, and K. Heyde, Phys. Rev. C **25**, 650 (1982).

[42] H. Bateman, Proc. Cambridge Philos. Soc **15**, 423 (1910).

[43] J. Cetnar, Annals of Nuclear Energy **33**, 640 (2006).

[44] W.-M. Yao *et al.*, J. Phys. G: Nucl. Part. Phys. **33**, 1 (2006).

[45] J. C. Hardy and I. S. Towner, Phys. Rev. C **71**, 055501 (2005).

[46] G. Alaga, K. Alder, A. Bohr, and B. Mottelson, Dan. Mat. Fys. Medd. **29**, (1955).

[47] J.-I. Fujita, G. T. Emery, and Y. Futami, Phys. Rev. C **1**, 2060 (1970).

[48] P. C. Sood, O. S. K. S. Sastri, and R. K. Jain, Eur. Phys. J. A **39**, 101 (2009).

[49] B. Singh, J. L. Rodriguez, S. S. M. Wong, and J. K. Tuli, Nuclear Data Sheets **84**, 487 (1998).

[50] N. Gove and M. Martin, At. Data Nucl. Data Tables **10**, 205 (1971).

[51] P. Hoff *et al.*, Phys. Rev. Lett. **77**, 1020 (1996).

[52] J. Kantele, *Handbook of Nuclear Spectrometry* (Academic Press, London, 1995).

[53] S. Svensson *et al.*, J. Electron Spectrosc. Related Phenom. **47**, 327 (1988).

[54] F. T. Porter, M. S. Freedman, and F. Wagner, Phys. Rev. C **3**, 2246 (1971).

[55] H. Primakoff and F. T. Porter, Phys. Rev. **89**, 930 (1953).

[56] T. Mukoyama and S. Shimizu, Phys. Rev. C **11**, 1353 (1975).

[57] M. S. Freedman, Annual Review of Nuclear Science **24**, 209 (1974).

[58] T. A. Carlson, W. E. Hunt, and M. O. Krause, Phys. Rev. **151**, 41 (1966).

[59] T. Kibédi *et al.*, Nucl. Instrum. Methods Phys. Res., Sect. A **589**, 202 (2008).

[60] V. Paar, Nuclear Physics A **331**, 16 (1979).

[61] C. J. Gallagher and S. A. Moszkowski, Phys. Rev. **111**, 1282 (1958).

[62] J. Suhonen, *From Nucleons to Nucleus: Concepts of Microscopic Nuclear Theory* (Springer, Berlin, 2007).

[63] H. Primakoff and S. P. Rosen, Annual Review of Nuclear and Particle Science **31**, 145 (1981).

[64] J. Ärje and K. Valli, Nuclear Instruments and Methods **179**, 533 (1981).

[65] J. Äystö *et al.*, Physics Letters B **138**, 369 (1984).

[66] J. Ärje *et al.*, Phys. Rev. Lett. **54**, 99 (1985).

[67] J. Ärje *et al.*, Nucl. Instrum. Methods Phys. Res., Sect. A **247**, 431 (1986).

[68] J. Ärje *et al.*, Nucl. Instrum. Methods Phys. Res., Sect. B **26**, 384 (1987).

[69] H. Penttilä *et al.*, Eur. Phys. J. A **44**, 147 (2010).

[70] P. Karvonen *et al.*, Nucl. Instrum. Methods Phys. Res., Sect. B **266**, 4794 (2008).

[71] E. Kugler, Hyperfine Interact. **129**, 23 (2000).

[72] P. Dendooven, Nucl. Instrum. Methods Phys. Res., Sect. B **126**, 182 (1997).

[73] J. Äystö, Nucl. Phys. A **693**, 477 (2001).

[74] A. Nieminen *et al.*, Phys. Rev. Lett. **88**, 094801 (2002).

[75] V. S. Kolhinen *et al.*, Nucl. Instrum. Methods Phys. Res., Sect. A **528**, 776 (2004).

[76] T. Eronen *et al.*, Nucl. Instrum. Methods Phys. Res., Sect. B **266**, 4527 (2008).

[77] A. Nieminen *et al.*, Nucl. Instrum. Methods Phys. Res., Sect. A **469**, 244 (2001).

[78] L. S. Brown and G. Gabrielse, Rev. Mod. Phys. **58**, 233 (1986).

[79] L. S. Brown and G. Gabrielse, Phys. Rev. A **25**, 2423 (1982).

[80] G. Savard *et al.*, Phys. Lett. A **158**, 247 (1991).

[81] T. Eronen, Ph.D. thesis, University of Jyväskylä, 2008.

[82] V. Kolhinen, Ph.D. thesis, University of Jyväskylä, 2003.

[83] G. Gräff, H. Kalinowsky, and J. Traut, Z. Phys. A **297**, 35 (1980).

[84] M. König *et al.*, Int. J. Mass Spectrom. Ion Processes **142**, 95 (1995).

[85] S. George *et al.*, Phys. Rev. Lett. **98**, 162501 (2007).

[86] S. George *et al.*, Europhys. Lett. **82**, 50005 (2008).

[87] H. Jorch and J. Campbell, Nuclear Instruments and Methods **143**, 551 (1977).

[88] J. Kalef-Ezra, Y. Horowitz, and J. Mack, Nucl. Instrum. Methods Phys. Res. **195**, 587 (1982).

[89] T. Tabata, R. Ito, and S. Okabe, Nucl. Instrum. Methods **94**, 509 (1971).

[90] J. Rissanen, Master thesis, JYFLTRAP:in soveltuvuus loukun sisäiseen spektroskopiaan, University of Jyväskylä, 2005.

[91] J. Kurpeta *et al.*, Acta Physica Polonica B **41**, 469 (2010).

[92] OriginPro software webpages, http://www.originlab.com/.

[93] J. Allison *et al.*, Nuclear Science, IEEE Transactions on nuclear science **53**, 270 (2006).

[94] MCNPX software webpages, https://mcnpx.lanl.gov/.

[95] J. Agramunt *et al.*, Nucl. Instrum. Methods Phys. Res., Sect. A, in preparation (2011).

[96] M. Gomez-Hornillos *et al.*, submitted to Hyperfine Interactions (2011).

[97] M. Gomez-Hornillos *et al.*, submitted to J. Phys.: Conference Series (2011).

[98] W. Urban *et al.*, Eur. Phys. J. A **22**, 157 (2004).

[99] SIMION software webpages, http://simion.com/.

[100] Y. X. Luo *et al.*, Phys. Rev. C **70**, 044310 (2004).

[101] W. Urban *et al.*, Eur. Phys. J. A **24**, 161 (2005).

[102] W. Urban *et al.*, Phys. Rev. C **82**, 064308 (2010).

[103] A. M. Bruce *et al.*, Phys. Rev. C **82**, 044312 (2010).

[104] Evaluated Nuclear Structure Data File (ENSDF), http://www.nndc.bnl.gov/ensdf/.

[105] A. Jokinen *et al.*, Nuclear Physics A **584**, 489 (1995).

[106] Q. Xu *et al.*, Phys. Rev. C **78**, 064301 (2008).

[107] J. C. Wang *et al.*, Eur. Phys. J. A **19**, 83 (2004).

[108] J. C. Wang *et al.*, Physics Letters B **454**, 1 (1999).

[109] J. A. Shannon *et al.*, Physics Letters B **336**, 136 (1994).

[110] P. Möller *et al.*, Phys. Rev. Lett. **97**, 162502 (2006).

[111] Q. H. Lu *et al.*, Phys. Rev. C **52**, 1348 (1995).

[112] R. Rodríguez-Guzmán, P. Sarriguren, L. Robledo, and S. Perez-Martin, Physics Letters B **691**, 202 (2010).

[113] L. Próchniak and S. G. Rohoziński, J. Phys. G: Nucl. Part. Phys. **36**, 123101 (2009).

[114] L. M. Robledo, R. Rodríguez-Guzmán, and P. Sarriguren, J. Phys. G: Nucl. Part. Phys. **36**, 115104 (2009).

[115] Hartree-Fock-Bogoliugov results, http://www.phynu.cea.fr.

[116] J. Hakala *et al.*, submitted to Eur. Phys. J. A (2011).

[117] E. Y. Yeoh *et al.*, Phys. Rev. C **83**, 054317 (2011).

[118] J. Q. Faisal *et al.*, Phys. Rev. C **82**, 014321 (2010).

[119] J. Kurpeta *et al.*, Eur. Phys. J. A **31**, 263 (2007).

[120] S. G. Nilsson and I. Ragnarsson, *Shapes and Shells in Nuclear Structure* (Cambridge University Press, Cambridge, 1995).

[121] G. Simpson, private communication, 2011.

[122] P. Möller *et al.*, At. Data Nucl. Data Tables **94**, 758 (2008).

[123] J. Äystö *et al.*, Physics Letters B **201**, 211 (1988).

[124] P. Möller, J. Nix, W. Myers, and W. Swiatecki, At. Data Nucl. Data Tables **59**, 185 (1995).

[125] H. Hua *et al.*, Physics Letters B **562**, 201 (2003).

[126] T. Kutsarova *et al.*, Phys. Rev. C **58**, 1966 (1998).

[127] P. H. Regan *et al.*, Phys. Rev. C **55**, 2305 (1997).

[128] R. Krücken *et al.*, Phys. Rev. C **60**, 031302 (1999).

[129] X. Q. Zhang *et al.*, Phys. Rev. C **61**, 014305 (1999).

[130] D. Fong *et al.*, Phys. Rev. C **72**, 014315 (2005).

[131] H. Penttilä, Ph. D. Thesis, University of Jyväskylä, (1992).

[132] B. Fogelberg *et al.*, Z. Phys. A **337**, 251 (1990).

[133] A. Algora *et al.*, Phys. Rev. Lett. **105**, 202501 (2010).